


Probing the order parameter symmetry of two-dimensional superconductors by twisted Josephson interferometry

Jiewen Xiao, Yaar Vituri, and Erez Berg

Department of Condensed Matter Physics, Weizmann Institute of Science, Rehovot 76100, Israel

 (Received 4 July 2023; revised 12 September 2023; accepted 14 September 2023; published 29 September 2023)

Probing the superconducting order parameter symmetry is a crucial step towards understanding the pairing mechanism in unconventional superconductors. Inspired by the recent discoveries of superconductivity in various van der Waals materials and the availability of the relative twist angle as a continuous tuning knob in these systems, we propose a general setup for probing the order parameter symmetry of two-dimensional superconductors in twisted Josephson junctions. The junction is composed of an anisotropic s -wave superconductor as a probe and another superconductor with an unknown order parameter symmetry. Assuming momentum-resolved tunneling, we investigate signatures of different order parameter symmetries in the twist angle dependence of the critical current, the current-phase relations, and magnetic field dependence. As a concrete example, we study a twisted Josephson junction between NbSe₂ and magic angle twisted bilayer graphene.

DOI: [10.1103/PhysRevB.108.094520](https://doi.org/10.1103/PhysRevB.108.094520)

I. INTRODUCTION

Identifying the pairing symmetry of unconventional superconductors (SCs) is a central challenge in condensed-matter physics. This is often the key step towards understanding the pairing mechanism. The structure of the order parameter may be probed by various experimental techniques, divided into non-phase-sensitive and phase-sensitive methods. Non-phase-sensitive methods probe the excitation spectrum, searching for gapless (nodal) quasiparticles. Phase-sensitive techniques, such as Josephson interferometry [1–5], are based on the interference of the quantum-mechanical phase of the SC order parameter. These methods have been successfully applied to determine the nodal d -wave nature of the superconducting gap in the high- T_c cuprate SCs.

However, the order parameter symmetry of numerous SCs remains unknown. Among these are the recently discovered superconducting phases in graphene multilayers, including twisted bilayer graphene (TBG) [6–8], twisted trilayer graphene (TTG) [9,10], twisted structures with four and five layers [11,12], rhombohedral trilayer graphene (RLG) [13], and Bernal bilayer graphene (BLG) [14,15]. The presence of multiple electron flavors in these systems, including the valley, spin, and layer indices, gives rise to a rich phase space for electrons to pair [16–19]. In some of these systems, large violations of the Pauli limit have been observed [10–14], indicating triplet pairing. In TBG and TTG, scanning tunneling microscopy (STM) experiments [20,21] have found evidence for gap nodes. Combined with the transport evidence for rotational symmetry breaking in the SC state [22], these experiments indicate a non- s -wave pairing symmetry [16]. Planar Josephson junctions are considered in the TBG case, which further revealed the pairing nature [23–29].

Twisted Josephson junctions, in which two planar superconductors are rotated relative to each other, can provide information about the pairing symmetry. For instance, in a

twisted c -axis Josephson junction between high- T_c cuprates, the twist angle dependence of the critical current should reflect the d -wave symmetry of the order parameter [30–37]. Experimental results on such junctions have been inconsistent [38–41]; some experiments [39] have detected the predicted twisted angle dependence and others have not. Compared to cuprates, heterostructures of van der Waals (vdW) materials such as graphene and transition-metal dichalcogenides (TMDs) are better controlled, and clean interfaces exhibiting momentum-resolved tunneling have been demonstrated [42–44].

Here we propose a general setup for probing the pairing order parameter symmetry of 2D SCs by twisted Josephson interferometry, utilizing various symmetries of the system. As shown schematically in Fig. 1(a), the system is composed of an s -wave SC as a probe and another SC with an unknown order parameter symmetry in the other side of the junction. We focus on materials with C_3 symmetry, such as TMDs and graphene-based systems. Assuming momentum-resolved tunneling between the two layers, we demonstrate signatures of different order parameter symmetries, such as the twist angle dependence of the critical current, the current-phase relations, and the magnetic field dependence of the Josephson coupling. For example, combining a chiral order parameter SC with an s -wave probe generates a dominant third harmonic in the current-phase relation. However, applying a small in-plane Zeeman field breaks the C_3 symmetry and creates a linear-in-field first-harmonic Josephson coupling. As a concrete setup, we study a twisted junction between NbSe₂ as an s -wave probe and magic angle twisted bilayer graphene (MATBG) as the SC with an unknown order parameter symmetry.

The rest of this article is organized as follows: In Sec. II we present a symmetry argument based on the Ginzburg-Landau (GL) theory and a microscopic weak-coupling model. In Sec. III we demonstrate the probing principle in the twisted NbSe₂ and MATBG junction. Section IV presents in-plane

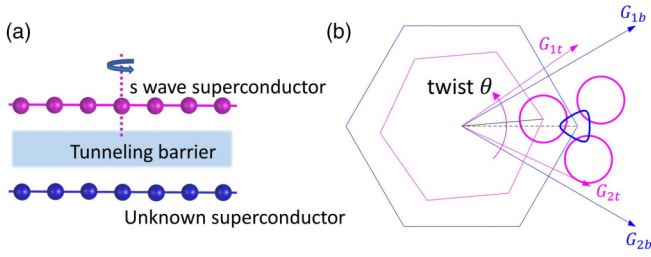


FIG. 1. Setup for probing the order parameter symmetry by twisted Josephson interferometry. (a) A Josephson junction between an s -wave SC probe (purple) and another SC system (blue) with an unknown order parameter symmetry. The two SCs are separated by a tunneling barrier. Both are assumed to have C_3 rotation symmetry. The top probe layer is rotated with respect to the bottom layer. (b) Fermi surfaces (FSs) and Brillouin zone alignment of the probe (top layer, purple) and system (bottom layer, blue). Reciprocal lattice vectors, $\mathbf{G}_{1,t/b}$ and $\mathbf{G}_{2,t/b}$, are denoted by purple/blue arrows, respectively. The Bragg scattered FSs of the probe (purple) are plotted around the system FS (blue) C_3 symmetrically. When twisting the probe, the probe FS is rotating and intersecting the system FS at different momenta.

magnetic-field-dependent Josephson couplings, and Sec. V proposes several experimental probing methods.

II. MODEL AND SYMMETRY ARGUMENTS

A. Ginzburg-Landau theory

Here we focus on the twisted Josephson junction in which both SCs are invariant under C_3 rotation symmetry and time-reversal symmetry (TRS). These symmetries apply to our primary example of a junction between graphene and TMD-based SCs. The superconducting order parameter belongs to one of the following irreducible representations of the C_3 group: A (one-dimensional representation, s -wave like) or E (two-dimensional representation, (p_x, p_y) or $(d_{x^2-y^2}, d_{xy})$ like).¹ We assume that spin-orbit coupling is present (provided by the TMD) and that there is no inversion symmetry; hence, singlet and triplet superconductivity are not distinct. For simplicity we will refer to the two representations as s wave or (p_x, p_y) wave, respectively. In the (p_x, p_y) case, we distinguish chiral $(p_x \pm ip_y)$ and nematic ($\alpha p_x + \beta p_y$, with $\alpha, \beta \in \mathbb{R}$) states. If the two SCs forming the junctions have mirror symmetry with respect to a common vertical plane, further distinctions are possible. The different order parameters considered in this work are summarized in Table I.

The lowest-order symmetry-allowed Josephson coupling terms between SCs with either of these order parameters and an s -wave SC as follows: (a) In the s -wave to s -wave case, both order parameters form the trivial representation under C_3 and the first-order term $\Delta_s^* \Delta_s$ is allowed. (b) In the s -wave

¹In cases where there is an additional C_2 , the A representation breaks into A_1 (even under C_2 , s -wave like) and A_2 (odd under C_2 , f -wave like), and similarly, E breaks into E_1 (even, $(d_{x^2-y^2}, d_{xy})$ like) and E_2 (odd, (p_x, p_y) like). These states remain distinct even in the absence of C_2 symmetry if the system is spin rotationally invariant, since one of them is a spin singlet and the other is a triplet.

TABLE I. Different order parameters and the corresponding lowest-order Josephson couplings.

Probe	System	Josephson coupling
s	s	$\Delta_s^* \Delta_s$
s	$p \pm ip$	$(\Delta_s^* \Delta_{p\pm})^3$
s	$p_{x,y}$, no mirror	$\Delta_s^* \Delta_{p_{x,y}}$
s	p_x , mirror	$\Delta_s^* \Delta_{p_x}$
s	p_y , mirror	$(\Delta_s^* \Delta_{p_y})^2$

to $p \pm ip$ -wave case, the C_3 symmetry is compatible with the chiral order parameter. Under C_3 operations, the n th-order term $(\Delta_s^* \Delta_{p\pm})^n$ accumulates a phase factor $e^{\pm i \frac{2\pi}{3} n}$. Therefore the lowest-order term coupling is $(\Delta_s^* \Delta_{p\pm})^3$, regardless of the rotation angle between two layers. Given the fact that third-order coupling is parametrically smaller than the first-order coupling in the perturbative tunneling regime, if we break the C_3 rotation symmetry it is possible to induce a first-order coupling larger in magnitude than the existing third order. Consider breaking of the C_3 symmetry by an externally applied magnetic field \mathbf{B} , we can write down the coupling terms in the Ginzburg-Landau (GL) free energy:

$$F = \alpha_B \Delta_s^* (\Delta_p \cdot \mathbf{B}) + \beta_B \Delta_s^* (\Delta_p \times \mathbf{B}) \cdot \hat{z} + \gamma (\Delta_s^* \Delta_p^+)^3 + \gamma (\Delta_s^* \Delta_p^-)^3 + \text{c.c.}, \quad (1)$$

where γ denotes the third-order C_3 symmetric coupling coefficient. α_B and β_B are the real coupling coefficients (Sec. IV). (c) For the s -wave to $p_{x,y}$ -wave case, the nodal order parameter breaks C_3 spontaneously; therefore C_3 symmetry should not be respected by the GL theory in this phase. The first-order term $\Delta_s^* \Delta_{p_{x,y}}$ is allowed for general twist angles. If we consider a case where both materials have mirror symmetry, the Josephson coupling should respect the mirror symmetry (D_1) when the two mirror planes are aligned. Under this condition, for the mirror-symmetric order parameter (denoted by Δ_{p_x} , mirror plane xz), the lowest-order coupling is still $\Delta_s^* \Delta_{p_x}$. For a mirror antisymmetric order parameter (denoted by Δ_{p_y}), the first-order coupling is forbidden, as it accumulates a π phase under the mirror. The lowest order of coupling is $(\Delta_s^* \Delta_{p_y})^2$. Similarly to the chiral case, we can induce a first-order harmonic by coupling to an external field. The symmetry-constrained Josephson couplings are summarized in Table I.

B. Microscopic weak-coupling model

The above symmetry argument is general for different types of SCs. Here we consider a simplified microscopic weak-coupling model to quantitatively describe Josephson couplings. This toy model well captures generic features of the twisted interface between TMDs (e.g., NbSe₂) and graphene-based SCs. A concrete example, NbSe₂ and MATBG twisted heterostructure, is considered in the next section. It shows consistent features compared to the toy model but gives quantitative magnitudes. Assuming momentum and spin-conserving single-electron tunneling element and singlet

pairing, the toy model Hamiltonian is

$$\mathcal{H} = \mathcal{H}_t + \mathcal{H}_b + T, \quad (2)$$

$$\mathcal{H}_l = \frac{1}{2} \sum_{\mathbf{p}} \Psi_{l,\mathbf{p}}^\dagger \begin{pmatrix} \epsilon_l(\mathbf{p}, \sigma) - \mu_l & i\sigma_y \Delta_l(\mathbf{p}) \\ -i\sigma_y \Delta_l^*(\mathbf{p}) & -(\epsilon_l^T(\mathbf{p}, \sigma) - \mu_l) \end{pmatrix} \Psi_{l,\mathbf{p}}, \quad (3)$$

$$T = \sum_{\{\mathbf{G}_t, \mathbf{G}_b\}} \sum_{\mathbf{p}, \sigma} t_{|\mathbf{p}|} c_{t,\mathbf{p},\sigma}^\dagger c_{b,\mathbf{p}',\sigma} + \text{H.c.}, \quad (4)$$

where $\Psi_{l,\mathbf{p}}^\dagger = (c_{l,\mathbf{p},\sigma}^\dagger, c_{l,\mathbf{p},\bar{\sigma}}^\dagger, c_{l,-\mathbf{p},\sigma}, c_{l,-\mathbf{p},\bar{\sigma}})$, and $c_{l,\mathbf{p},\sigma}$ annihilates a state with spin σ and momentum \mathbf{p} in layer l ($l = t, b$). The momentum \mathbf{p}' is determined by $\mathbf{p} + \mathbf{G}_t = R_\theta(\mathbf{p}' + \mathbf{G}_b)$. $\{\mathbf{G}_t, \mathbf{G}_b\}$ are the reciprocal lattice vectors in both layers (marked in Fig. 1), and R_θ is a c -axis rotation matrix (θ is the twist angle between two materials). In our convention the top layer $l = t$ is the probe (with an s -wave order parameter) and the bottom layer $l = b$ is the measured layer (with an unknown order parameter). The tunneling element $t_{|\mathbf{p}|}$ is assumed to decay fast with the in-plane momentum [45]. For the numerical analysis we assume the following low-energy dispersion: $\epsilon_t(\mathbf{p} = \mathbf{K}_t + \mathbf{k}, \sigma) = \lambda_t |\mathbf{k}|^2$ for the probe layer, and $\epsilon_b(\mathbf{p} = \mathbf{K}_b + \mathbf{k}, \sigma) = \lambda_{b0} |\mathbf{k}|^2 + \lambda_{b1} k_x (k_x^2 - 3k_y^2)$ for the measured layer. The momentum \mathbf{k} here is relative to the \mathbf{K}_l point of each layer l . The spectrum near the other valley $\mathbf{K}'_l = -\mathbf{K}_l$ is directly related by TRS. We use the lattice constants of NbSe₂ for the probe layer and graphene for the measured layer to determine the relative position and twist of valleys. Due to the fast decay of $t_{|\mathbf{p}|}$, we consider only Bragg scattering events within the first Brillouin zone (BZ) of the measured layer. The Fermi surfaces (FSs) of the probe (purple) and measured (blue) layers are shown in Fig. 1(b), with a twist angle of $\theta = 5^\circ$. This picture is in the normal state, without interlayer tunneling ($\Delta = 0, t = 0$). Turning on the pairing potential opens a gap at the FS. With the momentum-resolved tunneling, these band crossing points near the Fermi level contribute strongly to the phase dependence of the free energy [see Eq. (5)].

With the toy model Hamiltonian, we can write down the first- and higher-order Josephson couplings explicitly for different order parameter symmetries. Expanding the free energy to the second order in the tunneling element t (Appendix 1), the leading first-harmonic component is

$$\begin{aligned} F^{(1)} &= \frac{1}{\beta} \sum_{i,\mathbf{k}} \text{Tr}[G_b(\mathbf{k}) T_i G_t(\mathbf{k}_i) T_i^\dagger] \\ &= - \sum_{i,\mathbf{k},n} \frac{2|t_{\mathbf{k}}|^2 |\Delta_s| |\Delta_{\mathbf{k}}| \cos(\varphi + \alpha_{\mathbf{k}})}{\beta (|\Delta_{\mathbf{k}}|^2 + \omega_n^2 + \xi_{b,\mathbf{k}}^2) (|\Delta_s|^2 + \omega_n^2 + \xi_{t,\mathbf{k}_i}^2)} \\ &\stackrel{(\beta \rightarrow \infty)}{=} - \sum_{i,\mathbf{k}} \frac{|t_{\mathbf{k}}|^2 |\Delta_s| |\Delta_{\mathbf{k}}| \cos(\varphi + \alpha_{\mathbf{k}})}{E_{b,\mathbf{k}} E_{t,\mathbf{k}_i} (E_{b,\mathbf{k}} + E_{t,\mathbf{k}_i})}, \end{aligned} \quad (5)$$

where $\omega_n = (2n + 1)\pi/\beta$ is the Matsubara frequency and $\beta = 1/k_B T_{\text{temp}}$ (T_{temp} is the temperature). $G_l(\mathbf{k})$ is Green's function on layer l . $\xi_{l,\mathbf{k}} = \epsilon_{\mathbf{k}_l} - \mu_l$ and $E_{l,\mathbf{k}} = \sqrt{\xi_{l,\mathbf{k}}^2 + |\Delta_{l,\mathbf{k}}|^2}$. Δ_s is the top-probe-layer order parameter (assume to be momentum independent) and $\Delta_{\mathbf{k}}$ is the bottom-layer order parameter. φ is the relative phase between top and bottom SCs. $\alpha_{\mathbf{k}}$ is the momentum-dependent phase of the

unknown order parameter, for instance, $\alpha_{\mathbf{k}}^{(s)} = 0$ for s wave, $\alpha_{\mathbf{k}}^{(\text{nodal } p)} = \arg[\text{sgn}(\mathbf{k} \cdot \mathbf{n})]$ (where \mathbf{n} is the vector along the nodal direction) and $\alpha_{\mathbf{k}}^{(p \pm ip)} = \arg(k_x \pm ik_y)$ for $p \pm ip$ wave. $i \in 1, 2, 3$ is the Bragg scattering summation, where three processes are relevant within the first BZ of the measured layer.

In Eq. (5) we see that each \mathbf{k} point gives a finite contribution to the first harmonic. However, a nontrivial \mathbf{k} -dependent phase $\alpha_{\mathbf{k}}$ creates an interference effect upon integration over momenta and can lead to a vanishing coupling. For example, in the $p + ip$ case, using C_3 symmetry and the identity $\sum_{n=0}^2 \cos(\varphi + \frac{2\pi}{3}n) = 0$, Eq. (5) gives a vanishing first-order coupling, as expected from Table I. For higher-order terms, the nontrivial phase $\alpha_{\mathbf{k}}$ similarly enters the momentum integration and determines the leading harmonics (Appendix 1).

To quantitatively describe the probing principle, the Josephson current is numerically calculated by

$$\begin{aligned} F &= E_0 - \frac{2}{\beta} \sum_{\mathbf{k},n} \ln[\cosh(E_{\mathbf{k}n}/k_B T)], \\ I_{JJ} &= \frac{2e}{\hbar} \frac{dF}{d\varphi}, \end{aligned} \quad (6)$$

where E_0 is a phase-independent constant and $E_{\mathbf{k}n}$ is the n th positive-energy eigenvalue of the Bogoliubov–de Gennes (BdG) Hamiltonian H at momentum \mathbf{k} . Equation (6) is non-perturbative in the tunneling element t , which accounts for the cases when $t \lesssim |\Delta|$. All plotted results are at zero temperature. The Josephson current at twist angle $\theta = 1^\circ$ is shown in Fig. 2(a) for different order parameter symmetries. For the trivial s -wave– s -wave case, the first harmonic is the leading term, as expected. For the nodal order parameter Δ_{p_x} and Δ_{p_y} , the first-order term $\Delta_s^* \Delta_{p_{x/y}}$ is generally allowed but will be suppressed compared to the s -wave case due to the sign changing. If the first-order term is strongly suppressed, the second-order term from the Copper pair cotunneling $(\Delta_s^* \Delta_{p_{x/y}})^2$ shows up, since this term adds up constructively in momentum space. From Fig. 2(a) we indeed see a mixture of the first and second harmonics in both p_x and p_y cases. Since the toy model has mirror symmetry (mirror plane xz) and Δ_{p_y} is odd under the mirror, it leads to perfect cancellation of the first-order component when two mirror planes are aligned ($\theta = 0^\circ$). Even twisted $\theta = 1^\circ$ away, we still see a strong second-order Josephson component. On the other hand, the p_x wave is even under the mirror and the first harmonic is dominant near the zero twist angle. For the chiral $p + ip$ order parameter, only the $\sin(3\varphi)$ component exists.

Figure 2(b) shows the twist angle dependence of different harmonic components (first, second, and third) in the current-phase relation. For different order parameter symmetries, the amplitudes all drop down around a twist angle of $\theta = 15^\circ$. This is because two FSs do not overlap for larger twist angles. We also plot the normal-state conductance G versus twist angle in units of $2eI_c(\theta = 0^\circ)/\pi \Delta_s$ [left panel, Fig. 2(b)]. From the Ambegaokar-Baratoff (AB) relation [46], the normal-state conductance and the critical current between two s -wave SCs should obey $I_c/G = \pi \Delta_s/2e$. In our case the in-plane

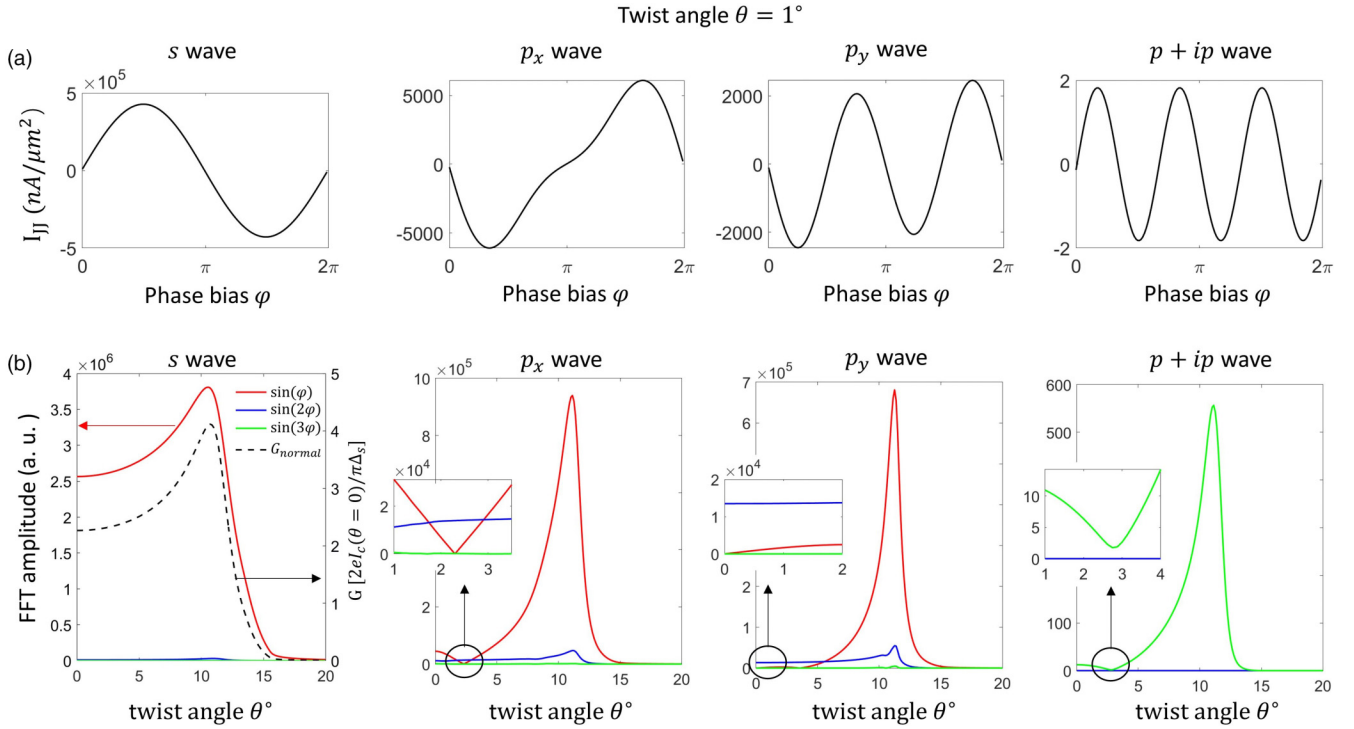


FIG. 2. Toy model results. (a) Josephson current at twist angle $\theta = 1^\circ$ for s , p_x , p_y , and $p + ip$ order parameters in the bottom layer. We used the following values for the model parameters: $\lambda_t = 5 \text{ eV \AA}^2$, $\lambda_{b0} = 1 \text{ eV \AA}^2$, $\lambda_{b1} = 1.5 \text{ eV \AA}^3$. The interlayer tunneling amplitude is $t = 1 \text{ meV}$. Chemical potentials are set to be $\mu_t = 600 \text{ meV}$ and $\mu_b = 40 \text{ meV}$. The gaps are $|\Delta_s| = |\Delta_k| = 5 \text{ meV}$. (b) Fast Fourier transform (FFT) amplitude of the current-phase relation vs the twist angle θ . FFT amplitudes of different harmonics up to the third order are plotted for s , p_x , p_y , and $p + ip$ cases. In the s -wave panel, we plot the normal-state conductance G as a function of the twist angle. G is plotted in units of $\frac{2eI_c(\theta=0)}{\pi\Delta_s}$. Inset of the p_x -wave case: the first-order harmonics vanish around twist angle 2.3° , and the second-order term becomes the leading order, with a sign that leads to spontaneous TRS breaking. Inset of the p_y -wave case: the first-order harmonics vanish at zero twist angle and then start rising when rotating away. Inset of the $p + ip$ wave case: there is a local minimum of critical current in the third harmonics, but it does not vanish.

momentum is conserved (contrary to the assumption used in the derivation of the AB relation). Nevertheless, we find that in the s -wave case, the ratio G/I_c is approximately constant as the twist angle varies. This is apparent in Fig. 2(b), where $I_c(\theta)$ and $G(\theta)$ are seen to follow a similar twist angle dependence. This is not the case for non- s -wave order parameter symmetries.

For the chiral $p + ip$ order parameter, only the $\sin(3\varphi)$ component exists for all twist angles, as we predicted by symmetry. The variation of the fast Fourier transform (FFT) amplitude depends on the band alignments.

Noticeably, for the p_x -wave case, we see a V-shaped drop of the first-order term around twist angle 2.3° . At this angle the first-order term vanishes due to destructive interference, and the second-order coupling is dominant [Fig. 2(b), inset]. The second-order term here has a negative sign, which gives a free-energy minimum at nonzero phase bias $\varphi \neq 0$, implying TRS breaking [32]. Note that this V-shaped drop happens at a generic angle and depends on band alignment details and not symmetry considerations. It serves as a signature of a sign-changing order parameter, even in the absence of mirror symmetry. Close to the perfect vanishing angle, the TRS breaking due to the comparable mixture of first and second harmonics can be detected by the Josephson diode effect [47]. Assuming higher-order terms are negligible, there is a

one-to-one correspondence between the amount of asymmetry in the critical current to the ratio between the first- and second-harmonic magnitudes (Appendix 7).

III. USING NbSe_2 TO PROBE THE ORDER PARAMETER OF MATBG

The toy model demonstrates how different order parameter symmetries of the system manifest themselves in the angle-dependent current-phase relation of the twisted junction. In order to provide quantitative predictions, we now study a concrete example: twisted Josephson junction between NbSe_2 , acting as an s -wave SC probe, and MATBG, an SC with an unknown order parameter symmetry. The two SCs are separated by two layers of WSe_2 that serve as a tunneling barrier. The barrier suppresses the interlayer hybridization and charge transfer, as confirmed by DFT calculations (Appendix 4), such that the MATBG layer is not strongly perturbed by the NbSe_2 . For simplicity, we consider monolayer NbSe_2 as a probe.

The MATBG layer is described by the continuum model [45]. NbSe_2 is considered by a three-orbital tight-binding model with the orbital basis $d_{z^2, \uparrow/\downarrow}$, $d_{xy, \uparrow/\downarrow}$, and $d_{x^2-y^2, \uparrow/\downarrow}$ [48]. The Josephson current is calculated by including a mean-field pairing potential in each layer and momentum-resolved

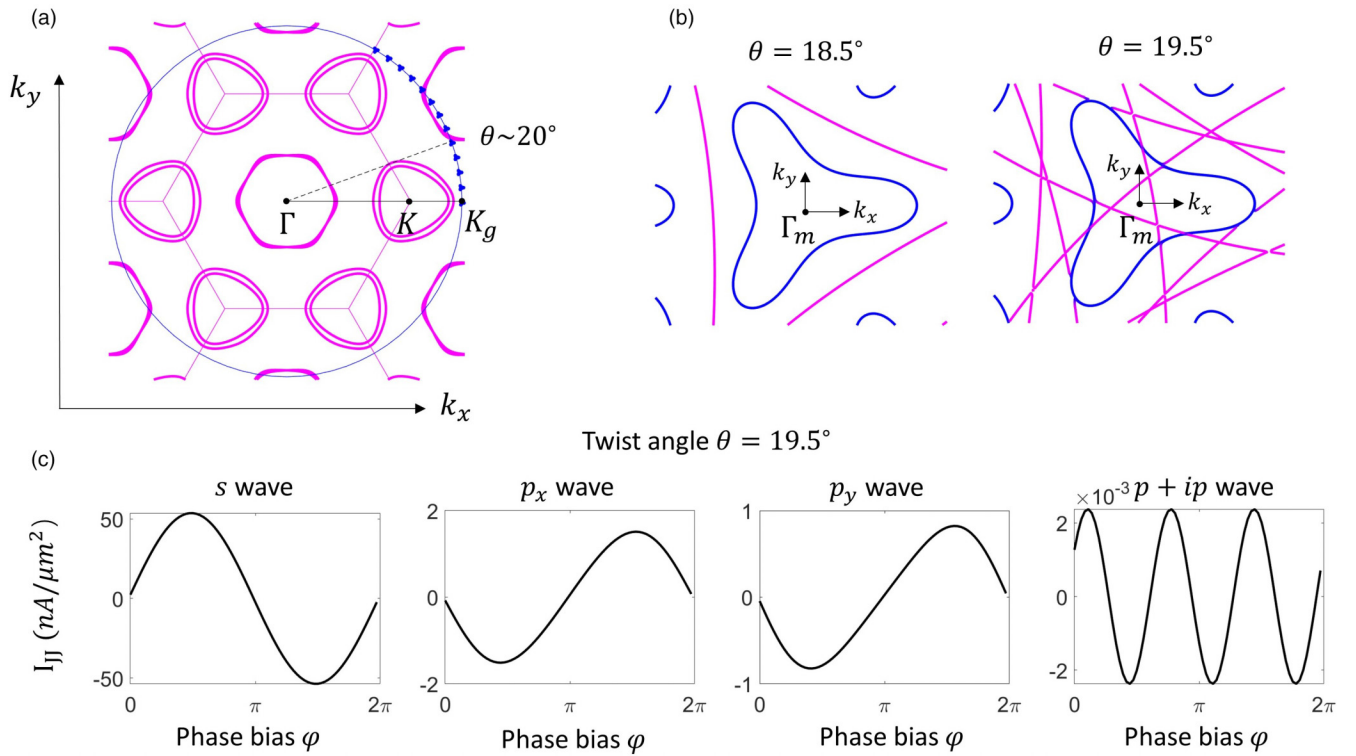


FIG. 3. NbSe₂-MATBG twisted heterostructure. (a) FS alignment between NbSe₂ and MATBG, over a 60° range of rotation angle. Here we use the crystalline axes of the NbSe₂ layer as our reference frame. Purple pockets are from NbSe₂ and small blue pockets are from MATBG. K is the valley of NbSe₂, and K_g is the valley of graphene. For MATBG, the Fermi level is set to $\mu = 5$ meV relative to charge neutrality, corresponding to a carrier density of $\sim 1.3 \times 10^{12}$ cm⁻² (assuming that all four flavors are filled equally). (b) Zoom in of the FSs at twist angles $\theta = 18.5^\circ$ and $\theta = 19.5^\circ$. Γ_m is the center of the mini-Brillouin zone. (c) The current-phase relation at twist angle $\theta = 19.5^\circ$ for different order parameter symmetries in the MATBG: s , p_x , p_y , and $p + ip$.

tunneling between the two SCs, with a tunneling element $t = 0.1$ meV (Appendix 2).

The FSs of the twisted junction are shown in Fig. 3(a). NbSe₂ has two types of electron pockets (purple) around the Γ point, K and K' point. The strong Ising spin-orbit coupling (SOC) in the probe splits the spin-up and spin-down components (Appendixes 2 and 5). The FSs of MATBG (blue) are also plotted, where we show the trajectory of the MATBG FS as the twist angle between the two SCs changes from 0° to 60°. Around $\theta = 20^\circ$, the Γ pocket of the NbSe₂ from the second BZ intersects the MATBG FS and gives a complicated band alignment, as shown in Fig. 3(b) for $\theta = 18.5^\circ$ and $\theta = 19.5^\circ$.

Figure 3(c) shows the current-phase relations for different order parameter symmetries at twist angle $\theta = 19.5^\circ$. An s -wave order parameter gives a trivial $\sin(\varphi)$ dependence. The magnitude of the critical current is around 50 nA/μm², which is much larger than the critical current for non- s -wave pairing symmetries. For p_x and p_y -wave cases, a mixture of first- and second-order harmonics is observed, with a magnitude of around 2 nA/μm². For the chiral case, the lowest order of Josephson coupling is $\sin(3\varphi)$, with a magnitude of around 2 pA/μm². If the interlayer coupling is increased by using a thinner tunneling barrier or by applying pressure to the junction, the third-order Josephson coupling is strongly enhanced (as it scales as t^6). For instance, by increasing t from 0.1 to 0.4 meV, Josephson current is increased by more than three

orders of magnitude (Appendix 3) and can reach the order of a few nA/μm².

The Josephson coupling has a complicated twist angle dependence. Figures 4(a) and 4(b) show the Josephson current as a function of phase bias and twist angle for the chiral $p + ip$ and nodal p_x wave cases, respectively. For a p_x order parameter, due to TRS, the current-phase relation is odd with respect to $\varphi \rightarrow -\varphi \text{ mod}(2\pi)$, i.e., the free energy $F(\varphi)$ is even. This does not apply in the $p + ip$ case, since this order parameter breaks TRS and leads to a phase shift $I(\varphi = 0) \neq 0$ in the current-phase relation.

Figures 4(c) and 4(d) show the corresponding FFT amplitude of different harmonics versus the twist angle from $\theta = 19^\circ$ to $\theta = 20.5^\circ$. For $p + ip$, the lowest order is $\sin(3\varphi)$, but its magnitude varies with the twist angle. In the plotted angle range we see two strong peaks. These peaks occur when the FSs of MATBG and NbSe₂ are tangent to each other, as shown in Fig. 4(e).

For the nodal p_x wave case, the first-order component generally dominates. There are several sign changes. Around them, the FFT amplitude shows sharp V-shaped drops in the first harmonic. Figure 4(f) shows a zoom in of one of these drops, where the first-order component vanishes but the $\sin(2\varphi)$ component survives. This feature is well captured by the toy model and occurs quite generally here, given the complicated band cutting conditions. As in the toy model, the sign of the second-harmonic term is such that it favors

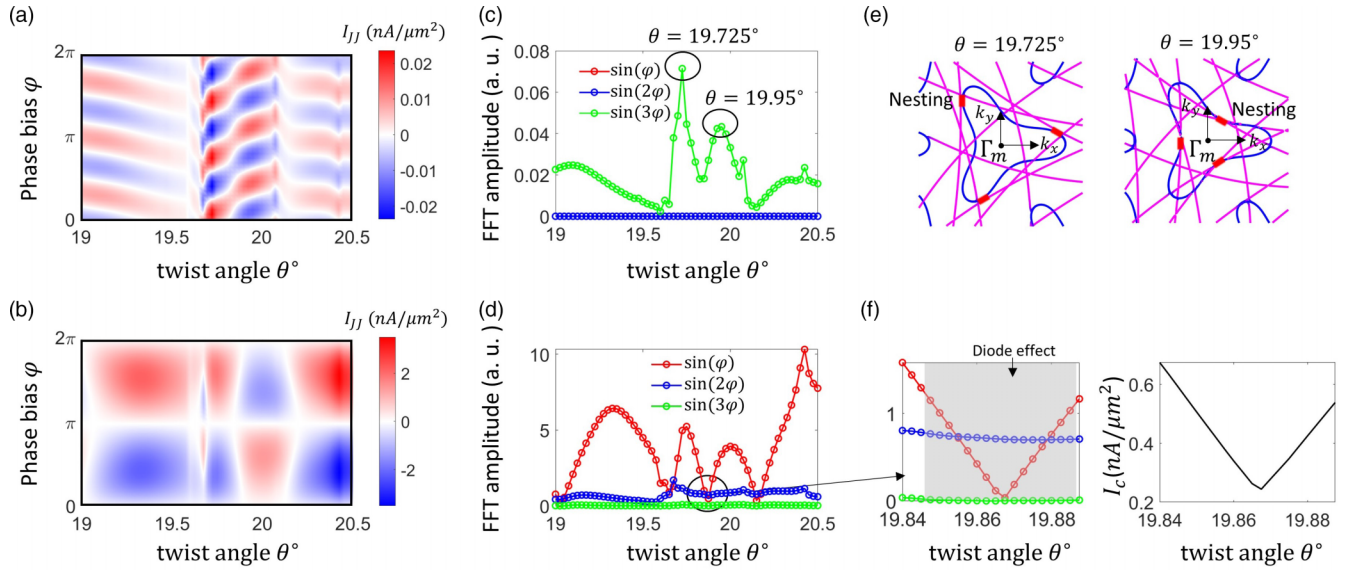


FIG. 4. Twist-angle-dependent Josephson current in the NbSe₂-MATBG heterostructure. (a), (b) Color map of the Josephson current as a function of twist angle and phase bias for $p + ip$ and p_x order parameter in the MATBG, respectively. (c), (d) The FFT amplitude of the current-phase relations as a function of twist angle for $p + ip$ and p_x order parameters. (e) The FSs at two twist angles from panel (c). The FSs of NbSe₂ and MATBG are tangent to each other (marked in red). In (f), a zoom-in FFT amplitude and critical current of the p_x wave order parameter around twist angle 19.88° is shown. The first-order component vanishes. In the shaded area, the Josephson diode effect can be observed.

time-reversal symmetry breaking (similarly to Ref. [32]). In the shaded region in Fig. 4(f) we expect to see a Josephson diode effect [47] (Appendix 7).

IV. IN-PLANE MAGNETIC-FIELD-INDUCED JOSEPHSON COUPLINGS

For the chiral order parameter, we have shown a robust $\sin(3\varphi)$ dependence in the current-phase relation, regardless of the twist angle, as long as the C_3 symmetry is maintained. The third-order harmonic scales as the interlayer tunneling amplitude t to the sixth power in the perturbative limit. On the other hand, if we slightly break the C_3 symmetry (either by an in-plane magnetic field or by strain), we can generate a first-order component that scales as t^2 , which can be more significant than the intrinsic third-order coupling. Phenomenologically, the phase-dependent free-energy term is given in Eq. (1).

Microscopically, an in-plane magnetic field generates both the Zeeman effect and the orbital effect. For a material with Rashba SOC, the Zeeman effect distorts the energy bands in a way that breaks the C_3 symmetry. By introducing these effects in the toy model, the Josephson current to the second order in t has the form (Appendix 5)

$$I^{(1)} = \sum_{\mathbf{k}} [I_{0\mathbf{k}} + I_{1\mathbf{k}}(\mathbf{B})] \cos(\varphi + \alpha_{\mathbf{k}} + \beta_{\mathbf{k},\mathbf{B}}), \quad (7)$$

where $\alpha_{\mathbf{k}}$ is the order parameter's momentum-dependent phase and φ is the phase difference between two SCs. $I_{0\mathbf{k}}$ is independent of the Zeeman field and is invariant under C_3 rotations. $I_{1\mathbf{k}}$ is a function of $(\mathbf{k} \cdot \mathbf{B})^2$, $(\mathbf{k} \times \mathbf{B})^2$, $|\mathbf{B}|^2$. There is also a phase shift $\beta_{\mathbf{k},\mathbf{B}} = b_{\mathbf{k}}(\mathbf{k} \cdot \mathbf{B})$, linear in $|\mathbf{B}|$ to the leading order. The coupling coefficient $b_{\mathbf{k}}$ is composed of microscopic parameters such as SOC strength and momenta.

For the trivial s -wave case, $\alpha_{\mathbf{k}}$ is a constant and the integration over momentum gives a nonvanishing first order at zero field. With an existing first-order component, both the phase shift $\beta_{\mathbf{k},\mathbf{B}}$ and $I_{1\mathbf{k}}$ term from the Zeeman field only generates a $|\mathbf{B}|^2$ -dependent critical current. However, for the chiral order parameter, the first-order term vanishes at zero field due to the negative interference in the momentum space. When Zeeman field generates a phase shift $\beta_{\mathbf{k},\mathbf{B}}$, it translates into a linear-in- $|\mathbf{B}|$ first-harmonic component in the current-phase relation (Appendix 5).

In the twisted NbSe₂-MATBG junction as an example, Figs. 5(a) and 5(b) show the current-phase relation and FFT amplitudes at twist angle $\theta = 19.5^\circ$ for different in-plane Zeeman field strengths (the calculation is described in Appendix 2). A $p + ip$ order parameter is assumed in the MATBG. At zero field there is only a $\sin(3\varphi)$ component. As the field increases a $\sin(\varphi)$ component is generated whose amplitude is linear in the field strength.

Next we consider the orbital effect of the magnetic field. In an infinite junction, assuming fully momentum-resolved tunneling, an arbitrarily small in-plane field completely decouples the order parameters of the two SCs. This is because the field creates a momentum mismatch between the two SC order parameters across the junction. If we relax the momentum conservation, assuming instead that the tunneling conserves momentum only up to $1/L$ (where L is the lateral size of the junction), we find a symmetry-breaking-induced first harmonic that is proportional to Φ^2 , where Φ is the flux through the junction. This is true for all orders in perturbation theory in t (Appendix 5). Therefore we expect the linear term related to the interplay of the Zeeman effect and Rashba SOC to dominate at small in-plane fields.

Another way to create an orbital effect that breaks the symmetry is to drive an in-plane supercurrent through one

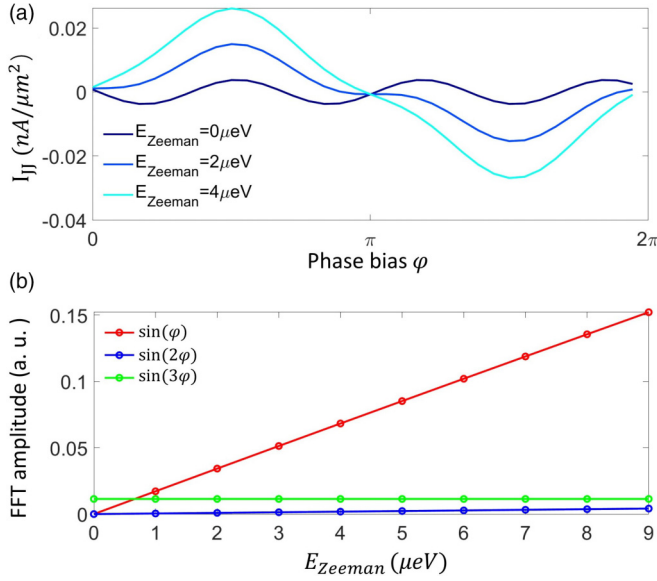


FIG. 5. Zeeman-field-induced Josephson coupling for a $p + ip$ order parameter in the probed layer. (a) The current-phase relation at twist angle $\theta = 19.5^\circ$ for different Zeeman field strengths. (b) The FFT amplitudes of the first, second, and third harmonics of the current-phase relation vs the Zeeman field strength.

of the SCs. Then the order parameter in that layer acquires finite momentum $2\mathbf{q}$ which results in a similar effect to that of the in-plane magnetic field. It also generates an additional symmetry-breaking effect from a shift of the energy spectrum of the quasiparticles. However, this effect does not contribute to the first-harmonic Josephson coupling in linear order in \mathbf{q} (Appendix 5).

V. DISCUSSIONS

We have studied how different order parameter symmetries of two-dimensional SCs manifest themselves in a twisted Josephson junction with an anisotropic s -wave SC as a probe. For an s -wave order parameter, the critical current dependence on the twist angle is expected to closely follow the dependence of the normal-state conductance. Therefore a strong deviation from this dependence is an indicator of a sign-changing order parameter.

The inclusion of SOC does not change the symmetry considerations, since we only assume C_3 rotational symmetry and TRS. Specifically, we have not assumed an independent spin-rotation symmetry. In the case of either Ising or Rashba SOC in the probe material, the probe SC order parameter will have a spin-triplet component. The symmetry arguments still hold as long as the order parameter of the SC probe transforms trivially under C_3 rotation and does not break TRS.

The periodicity of the dominant term in the current-phase relation can be directly detected by Shapiro steps in the ac Josephson effect. Instead of integer steps in the dc voltage from the current bias, $V_{dc} = n \frac{\hbar\omega_{ac}}{2e}$, we expect to see fractional steps, $V_{dc} = \frac{n}{m} \frac{\hbar\omega_{ac}}{2e}$, for a $\sin(m\varphi)$ term. A further discussion of the fractional Shapiro steps, including estimates for experimental parameters where they may be observed, is provided in Appendix 6.

For nodal order parameters the Hamiltonian has TRS and the current-phase relation is odd with respect to $\varphi \rightarrow -\varphi \bmod(2\pi)$, i.e., $I(\varphi = 0) = 0$. We predict the suppression of the first-order Josephson coupling at generic twist angles (not necessarily dictated by symmetry). The first-order coupling shows V-shaped drops versus the twist angle. Around these angles, the energy-phase relation is expected to be dominated by the second harmonic. Generically, the second-order Josephson coupling has a sign that favors TRS breaking (i.e., the minimum of the energy occurs away from 0 and π) [32]. We show that an asymmetry in the critical current is expected in this case (the so-called Josephson diode effect). Note that TRS breaking is necessary but not sufficient to get a Josephson diode effect. Multiple nonzero harmonic components are needed to generate the diode effect [49].

The direct measurement of the angle-dependent critical current is also interesting. For the specific NbSe₂-MATBG case, a strong enhancement of the critical current is predicted between twist angle $\theta = 20^\circ$ and $\theta = 40^\circ$. In this twist angle range, the large NbSe₂ FSs around the Γ point in the second BZ intersects the tiny FSs of the MATBG around the K point. A similar situation is expected in other graphene-based superconductors. The recently developed quantum twisting microscope [44] is a promising tool to study the twist-angle-dependent critical currents and current-phase relations, and identify different order parameter symmetries.

ACKNOWLEDGMENTS

We thank S. Ilani for stimulating discussions. This work was supported by the European Research Council (ERC) under the European Union's Horizon 2020 Research and Innovation Programme (Grant Agreement No. 817799), the US-Israel Binational Science Foundation (BSF), and the CRC 183 of the Deutsche Forschungsgemeinschaft (Project C02).

APPENDIX

1. Higher-order expansions from the toy model

In the toy model from Sec. II, the Green's function of the twisted junction is

$$G^{-1} = G_0^{-1} + T = \begin{pmatrix} G_b^{-1}(\mathbf{k}) & T_1(\mathbf{k}, \mathbf{k}_1) & T_2(\mathbf{k}, \mathbf{k}_2) & T_3(\mathbf{k}, \mathbf{k}_3) \\ T_1^\dagger(\mathbf{k}, \mathbf{k}_1) & G_l^{-1}(\mathbf{k}_1) & 0 & 0 \\ T_2^\dagger(\mathbf{k}, \mathbf{k}_2) & 0 & G_l^{-1}(\mathbf{k}_2) & 0 \\ T_3^\dagger(\mathbf{k}, \mathbf{k}_3) & 0 & 0 & G_l^{-1}(\mathbf{k}_3) \end{pmatrix}. \quad (\text{A1})$$

The diagonal part $G_l(\mathbf{k}) = H_l(\mathbf{k})^{-1}$, where H_l is the Hamiltonian in layer l . T is the off-diagonal part, the interlayer tunneling matrix. We assume $T_i = t\tau_3$, where τ_i are Pauli matrices that act in Nambu space. In the perturbative limit in t , we can expand the free energy as

$$F = -\frac{1}{\beta} \text{Tr}[\log[G_0^{-1}]] + \frac{1}{\beta} \sum_n \frac{1}{2n} \text{Tr}[G_0 T]^{2n}. \quad (\text{A2})$$

The leading first-harmonic term is

$$\begin{aligned}
F^{(1)} &= \frac{1}{2\beta} \text{Tr}[G_0 T]^2 = \frac{1}{\beta} \sum_{n, \mathbf{k}, j} \text{Tr}[G_b(\mathbf{k}, i\omega_n) T_j G_t(\mathbf{k}_j, i\omega_n) T_j^\dagger] = F_0^{(1)} - \sum_{n, \mathbf{k}, j} \frac{2|t|^2 |\Delta_{\mathbf{k}}| |\Delta_s| \cos(\alpha_{\mathbf{k}} + \varphi)}{\beta(\omega_n^2 + |\Delta_{\mathbf{k}}|^2 + \xi_{b, \mathbf{k}}^2)(\omega_n^2 + |\Delta_s|^2 + \xi_{t, \mathbf{k}_j}^2)} \\
&= F_0^{(1)} - \sum_{n, \mathbf{k}, j} \frac{|t|^2 |\Delta_{\mathbf{k}}| |\Delta_s|}{E_{b, \mathbf{k}}^2 - E_{t, \mathbf{k}_j}^2} \left[\frac{f(E_{b, \mathbf{k}}) - f(-E_{b, \mathbf{k}})}{E_{b, \mathbf{k}}} - \frac{f(E_{t, \mathbf{k}_j}) - f(-E_{t, \mathbf{k}_j})}{E_{t, \mathbf{k}_j}} \right] \cos(\alpha_{\mathbf{k}} + \varphi) \\
&\stackrel{(\beta \rightarrow \infty)}{=} F_0^{(1)} - \sum_{\mathbf{k}, j} \frac{|t|^2 |\Delta_{\mathbf{k}}| |\Delta_s|}{E_{b, \mathbf{k}} E_{t, \mathbf{k}_j} (E_{b, \mathbf{k}} + E_{t, \mathbf{k}_j})} \cos(\alpha_{\mathbf{k}} + \varphi), \tag{A3}
\end{aligned}$$

where ω_n is the Matsubara frequency and $f(E)$ is the Fermi-Dirac distribution function. $E_{l, \mathbf{k}} = \sqrt{\xi_{l, \mathbf{k}}^2 + |\Delta_l|^2}$, with $l = t/b$. The order parameter phase $\alpha_{\mathbf{k}} = 0$ for s -wave, $\alpha_{\mathbf{k}}^{(p_y)} = \arg[\text{sgn}(\mathbf{k} \cdot \mathbf{n})]$ and $\alpha_{\mathbf{k}}^{(p \pm ip)} = \arg(k_x \pm ik_y)$ for $p \pm ip$ wave. \mathbf{n} is the vector along the nodal direction. φ represents the phase difference between the two SCs, and j is the Bragg scattering summation. Within the first BZ of the measured layer, the momentum \mathbf{k} is coupled to three different momenta \mathbf{k}_j in the probe layer, related by Bragg scattering j . $F_0^{(1)}$ is the part of the free energy that does not depend on φ . In the last equation we have taken the zero-temperature limit, which gives Eq. (5) in the main text.

For the leading second-harmonic term, we have

$$\begin{aligned}
F^{(2)} &= \frac{1}{4\beta} \text{Tr}[G_0 T]^4 = \frac{1}{2\beta} \sum_{j_1, j_2, n, \mathbf{k}} \text{Tr}[G_b(\mathbf{k}, i\omega_n) T_{j_1} G_t(\mathbf{k}_{j_1}, i\omega_n) T_{j_1}^\dagger G_b(\mathbf{k}_{j_2}, i\omega_n) T_{j_2} G_t(\mathbf{k}_{j_3}, i\omega_n) T_{j_2}^\dagger] \\
&= F_0^{(2)} + \sum_{j_1, j_2, n, \mathbf{k}} \frac{|t|^4 |\Delta_{\mathbf{k}}| |\Delta_{\mathbf{k}_{j_2}}| |\Delta_s|^2 \cos(\alpha_{\mathbf{k}} + \alpha_{\mathbf{k}_{j_2}} + 2\varphi)}{\beta(\omega_n^2 + |\Delta_{\mathbf{k}}|^2 + \xi_{b, \mathbf{k}}^2)(\omega_n^2 + |\Delta_s|^2 + \xi_{t, \mathbf{k}_{j_1}}^2)(\omega_n^2 + |\Delta_{\mathbf{k}_{j_2}}|^2 + \xi_{b, \mathbf{k}_{j_2}}^2)(\omega_n^2 + |\Delta_s|^2 + \xi_{t, \mathbf{k}_{j_3}}^2)}, \tag{A4}
\end{aligned}$$

where j_1 and j_2 are Bragg scattering summations. Momentum \mathbf{k}_{j_3} is determined once specifying j_1 and j_2 processes. Here we only kept the phase-dependent second-harmonic Josephson couplings. The other terms are included in $F_0^{(2)}$ (a phase-independent term and also a correction to the first harmonic at fourth order in t). For the nodal order parameter p_y (odd under mirror) the first harmonic vanishes, as seen from Eq. (5) in the main text. For the second harmonic here, one possible term in Eq. (A4) is $\alpha_{\mathbf{k}_a} = \alpha_{\mathbf{k}_b} = \alpha_{\mathbf{k}}$, which gives the phase $\cos(2\alpha_{\mathbf{k}} + 2\varphi)$. In this case, inserting $\alpha_{\mathbf{k}}^{(p_y)} = \arg[\text{sgn}(\mathbf{k} \cdot \mathbf{n})]$ gives a nonvanishing second-harmonic coupling.

The leading third-harmonic coupling is generated at sixth order in t :

$$\begin{aligned}
F^{(3)} &= \frac{1}{6\beta} \text{Tr}[G_0 T]^6 = F_0^{(3)} \\
&- \sum_{j_1, j_2, j_3, n, \mathbf{k}} \frac{2|t|^6 |\Delta_{\mathbf{k}}| |\Delta_{\mathbf{k}_{j_2}}| |\Delta_{\mathbf{k}_{j_4}}| |\Delta_s|^3 \cos(\alpha_{\mathbf{k}} + \alpha_{\mathbf{k}_{j_2}} + \alpha_{\mathbf{k}_{j_4}} + 3\varphi)}{3\beta(\omega_n^2 + |\Delta_{\mathbf{k}}|^2 + \xi_{b, \mathbf{k}}^2)(\omega_n^2 + |\Delta_s|^2 + \xi_{t, \mathbf{k}_{j_1}}^2)(\omega_n^2 + |\Delta_{\mathbf{k}_{j_2}}|^2 + \xi_{b, \mathbf{k}_{j_2}}^2)(\omega_n^2 + |\Delta_s|^2 + \xi_{t, \mathbf{k}_{j_3}}^2)(\omega_n^2 + |\Delta_{\mathbf{k}_{j_4}}|^2 + \xi_{b, \mathbf{k}_{j_4}}^2)(\omega_n^2 + |\Delta_s|^2 + \xi_{t, \mathbf{k}_{j_5}}^2)}, \tag{A5}
\end{aligned}$$

where $j_{1,2,3}$ are Bragg scattering summations, and the momentum \mathbf{k}_{j_4} and \mathbf{k}_{j_5} are determined once specifying $j_{1,2,3}$ processes.

2. MATBG-NbSe₂ Josephson coupling

The MATBG layer is described by the continuum model [45]:

$$\mathcal{H}_{\text{MATBG}} = \mathcal{H}_t + \mathcal{H}_b + \mathcal{H}_{tb}, \tag{A6}$$

$$\mathcal{H}_t = \sum_{s, \xi, \mathbf{q}} a_{t, s, \xi}^\dagger(\mathbf{q}) \xi \hbar v_f \hat{\mathbf{R}}_+ \cdot \boldsymbol{\sigma} a_{t, s, \xi}(\mathbf{q}), \tag{A7}$$

$$\mathcal{H}_b = \sum_{s, \xi, \mathbf{q}} a_{b, s, \xi}^\dagger(\mathbf{q}) \xi \hbar v_f \hat{\mathbf{R}}_- \cdot \boldsymbol{\sigma} a_{b, s, \xi}(\mathbf{q}), \tag{A8}$$

$$\mathcal{H}_{tb} = \sum_{s, \xi, \mathbf{q}, \mathbf{q}'} a_{t, s, \xi}^\dagger(\mathbf{q}) T_{\mathbf{q}, \mathbf{q}'}^\xi a_{b, s, \xi}(\mathbf{q}'). \tag{A9}$$

Here $a_{t/b, s, \xi}^\dagger$ is a two-component spinor of creation operators for electrons in the two sublattices in the top or bottom (t or b) graphene layer, with spin s and valley ξ . $\hat{\mathbf{R}}_\pm = \cos \frac{\theta_{tbg}}{2} \pm i\sigma_y \sin \frac{\theta_{tbg}}{2}$ is the rotation matrix of the top/bottom graphene layer with a relative twist angle θ_{tbg} . v_f is the Fermi velocity of the graphene layer. σ^α are Pauli matrices that act in sublattice space. \mathbf{q} and \mathbf{q}' are electron momentum related by Bragg scatterings: $\mathbf{q} - \mathbf{q}' = \{\mathbf{q}_b, \mathbf{q}_{tr}, \mathbf{q}_{tl}\}$, where $\mathbf{q}_b = \frac{8\pi \sin \frac{\theta_{tbg}}{2}}{3\sqrt{3}a}(-1, 0)$, $\mathbf{q}_{tr} = \frac{8\pi \sin \frac{\theta_{tbg}}{2}}{3\sqrt{3}a}(\frac{\sqrt{3}}{2}, \frac{1}{2})$, $\mathbf{q}_{tl} = \frac{8\pi \sin \frac{\theta_{tbg}}{2}}{3\sqrt{3}a}(-\frac{\sqrt{3}}{2}, \frac{1}{2})$. a is the bond length in graphene. $T_{\mathbf{q}, \mathbf{q}'}^\xi$ is the interlayer tunneling matrix, given in Ref. [45].

NbSe₂ is modeled by a tight-binding model with three Nb d orbitals: $d_{z^2, \uparrow/\downarrow}$, $d_{xy, \uparrow/\downarrow}$, and $d_{x^2-y^2, \uparrow/\downarrow}$. The Slater-Koster hopping between these orbitals is given in Ref. [48].

The Josephson current of the twisted interface is calculated by including the pairing potential in each layer and also the momentum-resolved interlayer tunneling. The pairing potential is added in the BCS mean-field way. For NbSe₂ we use a constant superconducting gap $\Delta_s = 0.67$ meV. For MATBG, we assume the nodal and chiral order parameter takes the form

$$\Delta_{p_x} = \Delta_0 \cos(\alpha_{\mathbf{k}}), \quad (\text{A10})$$

$$\Delta_{p_y} = \Delta_0 \sin(\alpha_{\mathbf{k}}), \quad (\text{A11})$$

$$\Delta_{p \pm ip} = \Delta_0 e^{i\alpha_{\mathbf{k}}}, \quad (\text{A12})$$

with $\Delta_0 = 0.2$ meV. $\alpha_{\mathbf{k}}$ is the angle between \mathbf{k} and the x axis, measured relative to the center of mini-BZ.

The Cooper pair tunneling events include Bragg scatterings within the range of the first BZ of the graphene layer. Including the microscopic orbital symmetry, the largest interlayer coupling comes from the p_z orbital of graphene and d_{z^2} orbital of NbSe₂. The interlayer tunneling term is

$$\mathcal{H}_{\text{inter}} = \sum_{s,\xi,\mathbf{k},j,\sigma} a_{t,s,\xi,\sigma}^\dagger(\mathbf{k}) T_j^\sigma d_{z^2,s}(\mathbf{k}'), \quad (\text{A13})$$

$$T_j^\sigma = t e^{i\mathbf{G}_{T,j} \cdot \boldsymbol{\tau}_\sigma}. \quad (\text{A14})$$

σ is the sublattice index, with the corresponding sublattice vector $\boldsymbol{\tau}_\sigma$. j is the Bragg scattering processes, which relates momentum by

$$\mathbf{k} + \mathbf{K}_{\mathbf{g},\xi} + \mathbf{G}_{j,T} = \mathbf{k}' + \mathbf{G}_{j,\text{NbSe}_2}. \quad (\text{A15})$$

$\mathbf{G}_{j,T}$ and $\mathbf{G}_{j,\text{NbSe}_2}$ are reciprocal lattice vectors in the top graphene layer and NbSe₂, respectively. $\mathbf{K}_{\mathbf{g},\xi}$ is the K point of the top graphene.

To calculate the Zeeman-field-dependent Josephson coupling, we include Ising and Rashba SOC in the MATBG continuum model, with the SOC strength λ_{Ising} and $\lambda_{\text{Rashba}} = 1$ meV, consistent with the value reported in the literature [50]. Here, in this twisted Josephson junction setup, both the inserted WSe₂ tunneling barrier and NbSe₂ can generate SOC in MATBG.

3. Interlayer tunneling dependence of the Josephson coupling

As discussed in the main text, the critical current of a nontrivial order parameter can be enhanced by increasing the interlayer tunneling strength t . Figure 6 shows the critical current for the $p + ip$ case of the NbSe₂-MATBG twisted junction at twist angle $\theta = 19.5^\circ$. I_c is significantly increased to ~ 5 nA/ μm^2 when $t = 0.4$ meV. When increasing t from 0.05 meV to 0.3 meV, I_c scales approximately as t^6 , as expected.

4. Suppression of interlayer hybridization by tunneling barrier

We performed the density function theory (DFT) calculation using the Vienna ab initio Simulation Package (VASP) [51,52]. The exchange correlation is described by the Perdew-Burke-Ernzerhof (PBE) formulation under the generalized gradient approximation (GGA) [53]. Here we consider a heterostructure of monolayer NbSe₂-bilayer WSe₂-graphene, as

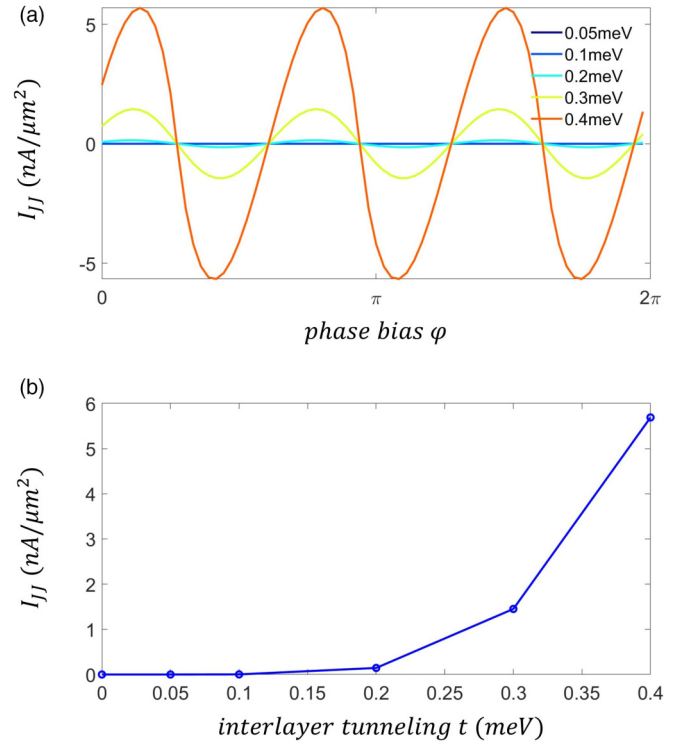


FIG. 6. Critical current dependence on the tunneling amplitude t in the case of a $p \pm ip$ order parameter in twisted NbSe₂-MATBG junction at $\theta = 19.5^\circ$. (a) The current-phase relation for different interlayer tunneling amplitude t . (b) The critical current vs t .

shown in Fig. 7(a). The band structure is shown in Fig. 7(b). The red and blue color represents the weight of wave function on NbSe₂ (red) and graphene (blue). In the low-energy region we see that the graphene Dirac cone approximately retains its original shape and is shifted by 35 meV due to the work-function differences, which can be gated to the charge neutrality. For the case of a few layers of graphene (such as MATBG), we expect the work-function differences to be of a similar magnitude.

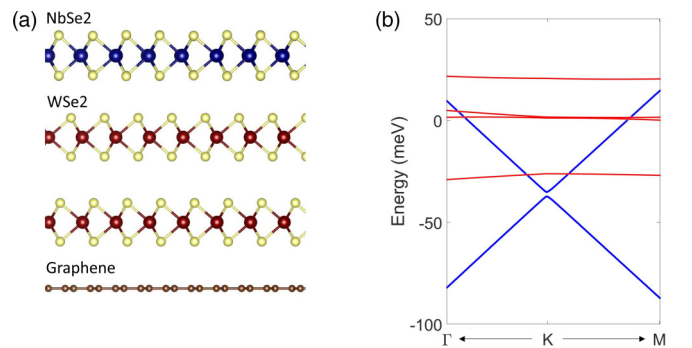


FIG. 7. (a) The monolayer NbSe₂-bilayer WSe₂-graphene heterostructure. (b) Band structure of the heterostructure. Red and blue colors represent the weight of the wave function on NbSe₂ (red) and graphene (blue). The WSe₂ bands are outside of the energy window shown here.

5. Magnetic-field-dependent Josephson couplings

a. Zeeman effect

Here we add Zeeman field, Rashba, and Ising SOC in the toy model to study the Zeeman-field-induced Josephson couplings. The toy model Hamiltonian is

$$\mathcal{H}_t = \frac{1}{2} \sum_{\mathbf{k}} \Psi_{t,\mathbf{k}}^\dagger \begin{pmatrix} \xi_t(\mathbf{k}, \sigma) + g_t \mathbf{B} \cdot \boldsymbol{\sigma} + \lambda_t \sigma_z & i\sigma_y \Delta_t(\mathbf{k}) \\ -i\sigma_y \Delta_t^*(\mathbf{k}) & -(\xi_t(-\mathbf{k}, \sigma) + g_t \mathbf{B} \cdot \boldsymbol{\sigma} - \lambda_t \sigma_z)^T \end{pmatrix} \Psi_{t,\mathbf{k}}, \quad (\text{A16})$$

$$\mathcal{H}_b = \frac{1}{2} \sum_{\mathbf{k}} \Psi_{b,\mathbf{k}}^\dagger \begin{pmatrix} \xi_b(\mathbf{k}, \sigma) + g_b \mathbf{B} \cdot \boldsymbol{\sigma} + \lambda_b \mathbf{k} \times \boldsymbol{\sigma} & i\sigma_y \Delta_b(\mathbf{k}) \\ -i\sigma_y \Delta_b^*(\mathbf{k}) & -(\xi_b(-\mathbf{k}, \sigma) + g_b \mathbf{B} \cdot \boldsymbol{\sigma} - \lambda_b \mathbf{k} \times \boldsymbol{\sigma})^T \end{pmatrix} \Psi_{b,\mathbf{k}}, \quad (\text{A17})$$

where H_t is the probe layer and H_b is the measured layer. $\Psi_{l,\mathbf{k}}^\dagger = (c_{l,\mathbf{k},\sigma}^\dagger, c_{l,\mathbf{k},\bar{\sigma}}^\dagger, c_{l,-\mathbf{k},\sigma}, c_{l,-\mathbf{k},\bar{\sigma}})$, and $c_{l,\mathbf{k},\sigma}$ annihilates a state with spin σ and momentum \mathbf{k} in layer l . The momentum \mathbf{k} is measured relative to the K point. The Ising SOC $\lambda_t \sigma_z$ is included in the probe layer, which mimics the strong Ising SOC in NbSe₂. The interlayer tunneling remains in the form of Eq. (4) in the main text. For simplicity, we do not consider Bragg scatterings in the analytical expression shown below, and momentum \mathbf{k} determines \mathbf{k}' by the relation $\mathbf{k} + \mathbf{K}_b = R(\theta)(\mathbf{k}' + \mathbf{K}_t)$. The second-order perturbation gives

$$\begin{aligned} F^{(1)} &= \frac{1}{\beta} \sum_{n,\mathbf{k}} \text{Tr}[G_b(\mathbf{k}, i\omega_n) T G_t(\mathbf{k}', i\omega_n) T^\dagger] \\ &= \sum_{\mathbf{k}, n=0}^{n=\infty} 8\Delta_b \Delta_t \mathfrak{R} \left[\frac{\cos(\varphi + \alpha_{\mathbf{k}})}{\beta f_1 f_2} \left[-(-g_t^2 |\mathbf{B}|^2 + \Delta_t^2 + \xi_t^2 + \lambda_t^2 + \omega_n^2)(-g_b^2 |\mathbf{B}|^2 + \Delta_b^2 + \xi_b^2 + \lambda_b^2 |\mathbf{k}|^2 + \omega_n^2) \right. \right. \\ &\quad \left. \left. + 4g_t \omega_n [\omega_n g_b |\mathbf{B}|^2 - i\xi_b \lambda_b (\mathbf{k} \times \mathbf{B})] \right] + \frac{4 \sin(\varphi + \alpha_{\mathbf{k}})}{\beta f_1 f_2} [\lambda_t \lambda_b (\mathbf{k} \cdot \mathbf{B}) (\xi_t g_b + \xi_b g_t)] \right], \end{aligned} \quad (\text{A18})$$

where

$$\begin{aligned} f_1 &= (g_t |\mathbf{B}|^2 + \omega_n^2 + \lambda_t^2 - \Delta_t^2 - \xi_t^2)^2 + 4(\Delta_t^2 \omega_n^2 + \Delta_t^2 \lambda_t^2 + \omega_n^2 \xi_t^2), \\ f_2 &= g_b^4 |\mathbf{B}|^4 + 2g_b^2 |\mathbf{B}|^2 (\omega_n^2 - \Delta_b^2 - \xi_b^2) + (\Delta_b^2 + \omega_n^2 + \xi_b^2 + \lambda_b^2 |\mathbf{k}|^2)^2 - 4\lambda_b^2 |\mathbf{k}|^2 \xi_b^2 \\ &\quad + 2g_b^2 \lambda_b^2 [(\mathbf{k} \cdot \mathbf{B})^2 - (\mathbf{k} \times \mathbf{B})^2] + 8i\omega_n \xi_b \lambda_b g_b (\mathbf{k} \times \mathbf{B}). \end{aligned} \quad (\text{A19})$$

We sum the Matsubara frequency in pairs: $\omega_n = (2n + 1)/\beta$ and $\omega_{-n-1} = -(2n + 1)/\beta$. To the lowest order in $|\mathbf{B}|$, the above Eq. (A19) can be written in the form

$$F^{(2)} = \sum_{\mathbf{k}} [F_{0\mathbf{k}} + F_{1\mathbf{k}} [(\mathbf{k} \cdot \mathbf{B})^2, (\mathbf{k} \times \mathbf{B})^2, |\mathbf{B}|^2]] \cos(\varphi + \alpha_{\mathbf{k}} + \beta_{\mathbf{k},\mathbf{B}}), \quad (\text{A20})$$

where $F_{0\mathbf{k}}$ is independent of the Zeeman field and has C_3 symmetry. $F_{1\mathbf{k}}$ is a function of $(\mathbf{k} \cdot \mathbf{B})^2$, $(\mathbf{k} \times \mathbf{B})^2$, $|\mathbf{B}|^2$, second order in $|\mathbf{B}|$. There is also a phase shift $\beta_{\mathbf{k},\mathbf{B}} = b_{\mathbf{k}}(\mathbf{k} \cdot \mathbf{B}) + \mathcal{O}(|\mathbf{B}|^2)$, where $b_{\mathbf{k}}$, obtained from combining the sine and the cosine in Eq. (A18), depends on microscopic parameters, e.g., momentum \mathbf{k} , $g_{t/b}$, and $\lambda_{t/b}$.

For the s -wave case, we have a constant $\alpha_{\mathbf{k}}$, which gives a nonzero $F^{(2)} = \sum_{\mathbf{k}} F_{0\mathbf{k}} \cos(\varphi)$ in the absence of Zeeman field. Given the existing first-order term, both the \mathbf{B} -induced $F_{1\mathbf{k}}$ term and the phase shift $\beta_{\mathbf{k},\mathbf{B}}$ give a $|\mathbf{B}|^2$ -dependent critical current.

For the $p + ip$ case, $\sum_{\mathbf{k}} F_{0\mathbf{k}} \cos(\varphi + \alpha_{\mathbf{k}})$ vanishes by C_3 symmetry. In the presence of an in-plane field, $\beta_{\mathbf{k},\mathbf{B}} = b_{\mathbf{k}}(\mathbf{k} \cdot \mathbf{B})$ destroys the destructive interference in the summation $\sum_{\mathbf{k}} F_{0\mathbf{k}} \cos(\varphi + \alpha_{\mathbf{k}} + \beta_{\mathbf{k},\mathbf{B}})$. As a result, a first-harmonic Josephson coupling with a magnitude proportional to $|\mathbf{B}|$ is generated [seen directly from Eq. (A20)].

b. Orbital effect

Here we derive the orbital effect of an in-plane magnetic field. If the tunneling between the two superconductors is perfectly momentum conserving, then any arbitrarily small in-plane orbital field completely decouples the two order parameters. To mimic the effect of the finite size of the system and the effect of disorder, we first relax the momentum conservation assumption made in Eq. (4), and instead, we write the tunneling element in the absence of magnetic field as $t(\mathbf{p}, \mathbf{p}') = t_{(\frac{\mathbf{p}+\mathbf{p}'}{2})} \cdot f(\mathbf{p} - \mathbf{p}')$. f is a real and symmetric function peaked at zero (taking f to be a δ function recovers the momentum-conserving limit). We assume an in-plane magnetic field and write the vector potential as $\mathbf{A} = z\mathbf{B} \times \hat{\mathbf{z}}$. The Hamiltonian is written as

$$\mathcal{H} = \mathcal{H}_t + \mathcal{H}_b + T, \quad (\text{A21})$$

where $\mathcal{H}_{t,b}$ are as defined in Eq. (3), and T is given by

$$T = \sum_{p,p'} T_{p,p'} = \sum_{p,p'} \sum_{G_1, G_2} t_{(\frac{\mathbf{p}+\mathbf{p}'}{2})} \Psi_{t,\mathbf{p}}^\dagger \begin{pmatrix} f(\tilde{\mathbf{p}} - \tilde{\mathbf{p}}' + \mathbf{q}) & 0 \\ 0 & -f(\tilde{\mathbf{p}}' - \tilde{\mathbf{p}} + \mathbf{q}) \end{pmatrix} \Psi_{b,\mathbf{p}'}, \quad (\text{A22})$$

where $\tilde{\mathbf{p}} = \mathbf{p} + G_1$, $\tilde{\mathbf{p}}' = \mathbf{p}' + G_2$, and $\mathbf{q} = \frac{e}{\hbar} d\mathbf{B} \times \hat{\mathbf{z}}$ is the momentum boost due to the magnetic field. d is the distance between the two SCs. Using the fact that f is symmetric, we can expand to first order:

$$T_{\mathbf{p},\mathbf{p}'} = \sum_{G_1, G_2} t_{\left(\frac{\tilde{\mathbf{p}}+\tilde{\mathbf{p}}'}{2}\right)} \Psi_{t,\mathbf{p}}^\dagger [f(\tilde{\mathbf{p}} - \tilde{\mathbf{p}}')\tau_z + \mathbf{q} \cdot \nabla f \tau_0] \Psi_{b,\mathbf{p}'}. \quad (\text{A23})$$

The n th contribution to the free energy is given by

$$F^{(n)} = \frac{1}{n\beta} \sum_{\{\mathbf{p}\}, \{\mathbf{p}'\}, \omega} \text{Tr} \left[\prod_{i=1}^n (T_{\mathbf{p}_i, \mathbf{p}'_{i-1}} G_t(\mathbf{p}_i, \omega) T_{\mathbf{p}_i, \mathbf{p}'_i} G_b(\mathbf{p}'_i, \omega)) \right]. \quad (\text{A24})$$

Using Eq. (A23) and the trace invariance to circular shifts we can show that its linear expansion in \mathbf{q} is given by

$$F^{(n)} = F^{(n)}(\mathbf{q} = 0) + \frac{1}{\beta} \sum_{\substack{\{\mathbf{p}\}, \{\mathbf{p}'\}, \omega, \\ G_1, G_2}} \text{Tr} \left[\left(t_{\left(\frac{\tilde{\mathbf{p}}_1 + \tilde{\mathbf{p}}'_1}{2}\right)} \mathbf{q} \cdot \nabla f(\tilde{\mathbf{p}}_1 - \tilde{\mathbf{p}}'_1) G_t(\mathbf{p}_1, \omega) T_{\mathbf{p}_1, \mathbf{p}'_1}^{q=0} G_b(\mathbf{p}'_1, \omega) \right. \right. \\ \left. \left. + T_{\mathbf{p}_1, \mathbf{p}'_n}^{q=0} G_t(\mathbf{p}_1, \omega) t_{\left(\frac{\tilde{\mathbf{p}}_1 + \tilde{\mathbf{p}}'_1}{2}\right)} \mathbf{q} \cdot \nabla f(\tilde{\mathbf{p}}_1 - \tilde{\mathbf{p}}'_1) G_b(\mathbf{p}'_1, \omega) \right) \prod_{i=2}^n (T_{\mathbf{p}_i, \mathbf{p}'_{i-1}}^{q=0} G_t(\mathbf{p}_i, \omega) T_{\mathbf{p}_i, \mathbf{p}'_i}^{q=0} G_b(\mathbf{p}'_i, \omega)) \right]. \quad (\text{A25})$$

Since we sum over all momenta and Matsubara frequency, we can use the following map for the second term in the parenthesis: $\omega \leftrightarrow -\omega$, $\mathbf{p}'_{i+1} \leftrightarrow \mathbf{p}'_{n-i}$, and $\mathbf{p}_{i+2} \leftrightarrow \mathbf{p}_{n-i}$ (\mathbf{p}_1 maps to itself) to get

$$\nabla_{\mathbf{q}} F^{(n)} = \frac{1}{\beta} \sum_{\substack{\{\mathbf{p}\}, \{\mathbf{p}'\}, \omega, \\ G_1, G_2}} t_{\left(\frac{\tilde{\mathbf{p}}_1 + \tilde{\mathbf{p}}'_1}{2}\right)} \nabla f(\tilde{\mathbf{p}}_1 - \tilde{\mathbf{p}}'_1) \text{Tr} \left[G_t(\mathbf{p}_1, \omega) T_{\mathbf{p}_1, \mathbf{p}'_1}^{q=0} G_b(\mathbf{p}'_1, \omega) \prod_{i=2}^n (T_{\mathbf{p}_i, \mathbf{p}'_{i-1}}^{q=0} G_t(\mathbf{p}_i, \omega) T_{\mathbf{p}_i, \mathbf{p}'_i}^{q=0} G_b(\mathbf{p}'_i, \omega)) \right. \\ \left. + T_{\mathbf{p}_1, \mathbf{p}'_1}^{q=0} G_t(\mathbf{p}_1, -\omega) G_b(\mathbf{p}'_n, -\omega) \prod_{i=n}^2 (T_{\mathbf{p}_i, \mathbf{p}'_i}^{q=0} G_t(\mathbf{p}_i, -\omega) T_{\mathbf{p}_i, \mathbf{p}'_{i-1}}^{q=0} G_b(\mathbf{p}'_{i-1}, -\omega)) \right]. \quad (\text{A26})$$

Performing a circular shift for the second term and using the fact that $G_t^\dagger(\mathbf{p}, \omega) = G_t(\mathbf{p}, -\omega)$, let us write it as

$$\nabla_{\mathbf{q}} F^{(n)} = \frac{1}{\beta} \sum_{\substack{\{\mathbf{p}\}, \{\mathbf{p}'\}, \omega, \\ G_1, G_2}} t_{\left(\frac{\tilde{\mathbf{p}}_1 + \tilde{\mathbf{p}}'_1}{2}\right)} \nabla f(\tilde{\mathbf{p}}_1 - \tilde{\mathbf{p}}'_1) \text{Tr}[M + M^\dagger], \quad (\text{A27})$$

where

$$M = G_t(\mathbf{p}_1, \omega) T_{\mathbf{p}_1, \mathbf{p}'_1}^{q=0} G_b(\mathbf{p}'_1, \omega) \prod_{i=2}^n (T_{\mathbf{p}_i, \mathbf{p}'_{i-1}}^{q=0} G_t(\mathbf{p}_i, \omega) T_{\mathbf{p}_i, \mathbf{p}'_i}^{q=0} G_b(\mathbf{p}'_i, \omega)). \quad (\text{A28})$$

Both $T_{\mathbf{p}, \mathbf{p}'}^{q=0}$ and $G_t(\mathbf{p}, \omega)$ are traceless and can be written as a sum of Pauli matrices in Nambu space. Hence M is given by a linear sum of products of an odd number of Pauli matrices. After summing over Matsubara frequencies, tracing over M gives a purely imaginary contribution. Using the fact that $\text{Tr}[M^\dagger] = \text{Tr}[M]^*$ we find that $\nabla_{\mathbf{q}} F^{(n)} = 0$.

c. In-plane current effect

A similar effect to that of an in-plane field can be obtained by driving an in-plane current through one of the SCs. In this case the order parameter acquires a finite momentum $\Delta_t(\mathbf{p}) \rightarrow \Delta_t(\mathbf{p}) e^{i2\mathbf{q} \cdot \mathbf{R}}$ (assuming current in the top layer, where \mathbf{R} is the center-of-mass coordinate). This modifies the BdG Hamiltonian of the top layer. The bottom Hamiltonian is left unchanged, and the interlayer tunneling $T_{\mathbf{p}, \mathbf{p}'}$ is modified in the same way as in the previous section, allowing for non-momentum-conserving tunneling between the two SCs. To lowest order in $\mathbf{q} = 0$, we can set $\mathbf{q} = 0$ in the tunneling matrix element (the linear in $\mathbf{q} = 0$ term from the matrix element was shown to vanish in the previous section). The Hamiltonian is given by

$$\mathcal{H} = \mathcal{H}_t + \mathcal{H}_b + T, \quad (\text{A29})$$

$$\mathcal{H}_t = \frac{1}{2} \sum_{\mathbf{p}} \Psi_{t,\mathbf{p}}^\dagger \begin{pmatrix} \xi_t(\mathbf{p} + \mathbf{q}, \sigma) & i\sigma_y \Delta_t(\mathbf{p}) \\ -i\sigma_y \Delta_t^*(\mathbf{p}) & -(\xi_t^T(-\mathbf{p} + \mathbf{q}, \sigma)) \end{pmatrix} \Psi_{t,\mathbf{p}}, \quad (\text{A30})$$

$$\mathcal{H}_b = \frac{1}{2} \sum_{\mathbf{p}} \Psi_{b,\mathbf{p}}^\dagger \begin{pmatrix} \xi_b(\mathbf{p}, \sigma) & i\sigma_y \Delta_b(\mathbf{p}) \\ -i\sigma_y \Delta_b^*(\mathbf{p}) & -(\xi_b^T(-\mathbf{p}, \sigma)) \end{pmatrix} \Psi_{b,\mathbf{p}}, \quad (\text{A31})$$

where $\Psi_{t,\mathbf{p}}^\dagger = (c_{t,\mathbf{p}+\mathbf{q},\sigma}^\dagger, c_{t,\mathbf{p}+\mathbf{q},\bar{\sigma}}^\dagger, c_{t,-\mathbf{p}+\mathbf{q},\sigma}, c_{t,-\mathbf{p}+\mathbf{q},\bar{\sigma}})$, $\Psi_{b,\mathbf{p}}^\dagger = (c_{b,\mathbf{p},\sigma}^\dagger, c_{b,\mathbf{p},\bar{\sigma}}^\dagger, c_{b,-\mathbf{p},\sigma}, c_{b,-\mathbf{p},\bar{\sigma}})$, \mathbf{p}' is defined as in Eq. (4), and T is as defined in Eq. (A22), substituting $\mathbf{q} = 0$. Expanding the free energy to second order in T and to first order in \mathbf{q} gives

$$F^{(1)} = \frac{1}{\beta} \sum_{\mathbf{p}, \mathbf{p}', \omega} \text{Tr}[G_b(\mathbf{p}, \omega) T_{\mathbf{p}, \mathbf{p}'} G_t(\mathbf{p}', \omega) T_{\mathbf{p}, \mathbf{p}'}]$$

$$= \sum_{\substack{\{\mathbf{p}\}, \{\mathbf{p}'\}, \omega, \\ G_1, G_2}} \frac{4[t_{(\frac{\mathbf{p}+\mathbf{p}'}{2})} f(\tilde{\mathbf{p}} - \tilde{\mathbf{p}}')]^2 |\Delta_s| |\Delta_{\mathbf{p}'}| \cos(\varphi + \alpha_{\mathbf{p}'})}{\beta (|\Delta_{\mathbf{p}'}|^2 + \omega_n^2 + \xi_{b,\mathbf{p}}^2) [E_{t,\mathbf{p}} + \nabla \xi_t(\mathbf{p}) \cdot \mathbf{q} - i\omega] [E_{t,\mathbf{p}} - \nabla \xi_t(\mathbf{p}) \cdot \mathbf{q} + i\omega]}.$$
 (A32)

The linear order term in \mathbf{q} vanishes.

6. Fractional Shapiro steps

To calculate the Shapiro steps, we use the resistively capacitance shunted junction (RCSJ) model [54]. The Josephson junction is described by a circuit composed of a Josephson element, resistor, and capacitor in parallel. This model gives the Josephson dynamics under microwave irradiation. Assuming the junction is current biased, we have

$$I_{\text{bias}} = I_{dc} + I_{ac} \cos(\omega t) = I_{JJ}(\varphi) + \frac{V_{JJ}}{R} + C \frac{dV_{JJ}}{dt},$$

$$V_{JJ} = \frac{\hbar}{2e} \frac{d\varphi}{dt},$$
 (A33)

where R and C are the junction resistance and capacitance. We input different current-phase relations for $I_{JJ}(\varphi)$ for different order parameter symmetries. Specifically, here we consider $\sin(3\varphi)$ case for the chiral order parameter and mixed first- and second-order harmonics case for the nodal order parameter. By solving Eq. (A33) numerically, we

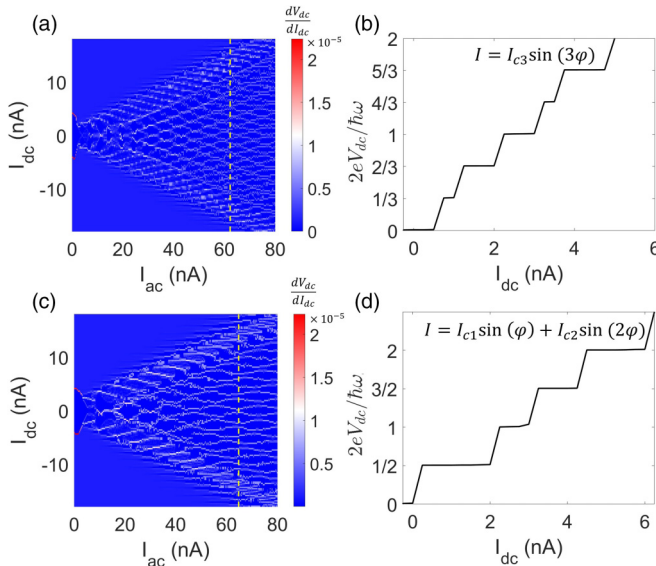


FIG. 8. Fractional Shapiro steps. (a) The $\frac{dV_{dc}}{dI_{dc}}$ signal vs I_{ac} and I_{dc} parameters in the current bias, with the current-phase relation $I(\varphi) = I_{c3} \sin 3\varphi$, $I_{c3} = 5$ nA. The parameters used in this calculation are given in the text. (b) V_{dc} as a function of I_{dc} at $I_{ac} = 65$ nA for the current-phase relation used in (a). (c) Same as (a) for the current-phase relation $I(\varphi) = I_{c1} \sin \varphi + I_{c2} \sin 2\varphi$, $I_{c1} = 2$ nA, $I_{c2} = 4$ nA. (d) V_{dc} as a function of I_{dc} at $I_{ac} = 65$ nA for the current-phase relation used in (c).

derive the junction dynamic behavior. As shown in Figs. 8(a) and 8(b), the $I_{JJ}(\varphi) = I_{c3} \sin(3\varphi)$ relation is reflected as fractional steps as $V_{dc} = \frac{n}{3} \frac{\hbar\omega}{2e}$. For the mixed case $I_{JJ}(\varphi) = I_{c1} \sin(\varphi) + I_{c2} \sin(2\varphi)$ in Figs. 8(c) and 8(d), we see half-integer steps as $V_{dc} = \frac{n}{2} \frac{\hbar\omega}{2e}$. Here, we used the following parameters: microwave angular frequency ~ 40 GHz, critical current ~ 5 nA/ μm^2 , normal-state resistance ~ 5 k $\Omega/\mu\text{m}^2$, and interlayer geometrical capacitance 20 fF/ μm^2 . The geometric capacitance is estimated from the interlayer distance $d \sim 2$ nm.

7. Josephson diode effect

In cases where time-reversal symmetry is spontaneously broken, the critical current through the junction can depend on

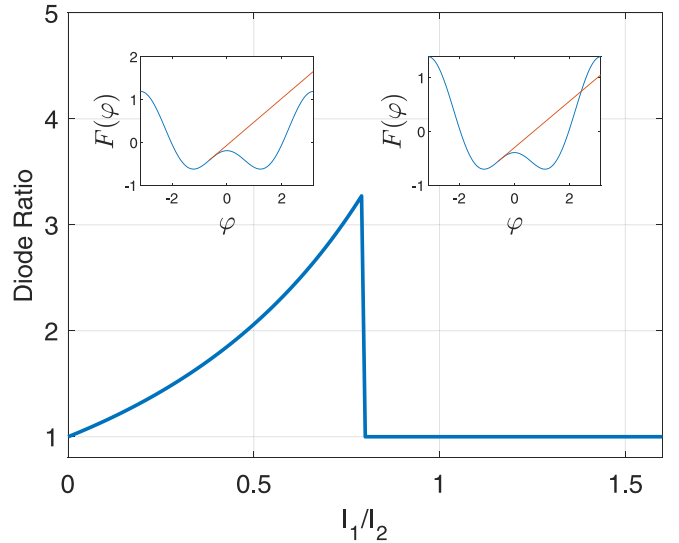


FIG. 9. Diode ratio for a junction with spontaneously broken TRS. We define the diode ratio as the ratio between the larger to the smaller critical current through the junction. Plotted here is the diode ratio as a function of the ratio between the first- and second-harmonic coefficients [$F = -I_1 \cos(\varphi) + (I_2/2) \cos(2\varphi)$]. Its maximal value is 3.27, obtained for $I_1/I_2 \approx 0.8$ (a larger diode can be achieved by including higher-order terms). For larger I_1/I_2 , the diode ratio is 1, since once the current exceeds the lower of the two critical currents near one of the minima and the phase is retrapped at the other minimum of $F(\varphi)$. The top-left inset shows $F(\varphi)$ as a function of relative phase for $I_1/I_2 < 0.8$, which results in a diode effect. The line in red is tangent to the free-energy curve which corresponds to the smaller of the two critical currents. The top right is for $0.8 < I_1/I_2 < 2$, where time reversal is broken but there is no diode effect.

the direction of the current [47]. We can define a measure of the asymmetry as the ratio between the two critical currents. An intuitive argument can be made regarding the possibility to have a diode effect using the washboard potential picture. Assuming that time-reversal symmetry is broken, the ground state has a phase difference φ which, in general, is neither 0 nor π . Around φ , the phase-dependent free energy $F(\varphi)$ is not symmetric. There are two points of maximal (minimal) slope which determine the externally applied current

required to drive the system out of the local minimum. Once the critical current is exceeded, the shape of $F(\varphi)$ could be such that the phase is retrapped in the other minimum (Fig. 9, top right) or the phase keeps increasing indefinitely under the influence of the dc current, corresponding to a dissipative state (Fig. 9, top left). In the case where retrapping occurs, since the total $F(\varphi)$ relation is time-reversal symmetric, the critical currents in the two directions are equal.

-
- [1] D. J. Van Harlingen, Phase-sensitive tests of the symmetry of the pairing state in the high-temperature superconductors: evidence for $d_{x^2-y^2}$ symmetry, *Rev. Mod. Phys.* **67**, 515 (1995).
- [2] C. Tsuei and J. Kirtley, Pairing symmetry in cuprate superconductors, *Rev. Mod. Phys.* **72**, 969 (2000).
- [3] S. Kashiwaya and Y. Tanaka, Tunnelling effects on surface bound states in unconventional superconductors, *Rep. Prog. Phys.* **63**, 1641 (2000).
- [4] Y. Tanaka and S. Kashiwaya, Theory of the Josephson effect in d -wave superconductors, *Phys. Rev. B* **53**, R11957 (1996).
- [5] Y. Tanaka and S. Kashiwaya, Theory of Josephson effects in anisotropic superconductors, *Phys. Rev. B* **56**, 892 (1997).
- [6] Y. Cao, V. Fatemi, S. Fang, K. Watanabe, T. Taniguchi, E. Kaxiras, and P. Jarillo-Herrero, Unconventional superconductivity in magic-angle graphene superlattices, *Nature (London)* **556**, 43 (2018).
- [7] Y. Cao, V. Fatemi, A. Demir, S. Fang, S. L. Tomarken, J. Y. Luo, J. D. Sanchez-Yamagishi, K. Watanabe, T. Taniguchi, E. Kaxiras *et al.*, Correlated insulator behaviour at half-filling in magic-angle graphene superlattices, *Nature (London)* **556**, 80 (2018).
- [8] M. Yankowitz, S. Chen, H. Polshyn, Y. Zhang, K. Watanabe, T. Taniguchi, D. Graf, A. F. Young, and C. R. Dean, Tuning superconductivity in twisted bilayer graphene, *Science* **363**, 1059 (2019).
- [9] J. M. Park, Y. Cao, K. Watanabe, T. Taniguchi, and P. Jarillo-Herrero, Tunable strongly coupled superconductivity in magic-angle twisted trilayer graphene, *Nature (London)* **590**, 249 (2021).
- [10] Y. Cao, J. M. Park, K. Watanabe, T. Taniguchi, and P. Jarillo-Herrero, Pauli-limit violation and re-entrant superconductivity in moiré graphene, *Nature (London)* **595**, 526 (2021).
- [11] J. M. Park, Y. Cao, L.-Q. Xia, S. Sun, K. Watanabe, T. Taniguchi, and P. Jarillo-Herrero, Robust superconductivity in magic-angle multilayer graphene family, *Nat. Mater.* **21**, 877 (2022).
- [12] G. W. Burg, E. Khalaf, Y. Wang, K. Watanabe, T. Taniguchi, and E. Tutuc, Emergence of correlations in alternating twist quadrilayer graphene, *Nat. Mater.* **21**, 884 (2022).
- [13] H. Zhou, T. Xie, T. Taniguchi, K. Watanabe, and A. F. Young, Superconductivity in rhombohedral trilayer graphene, *Nature (London)* **598**, 434 (2021).
- [14] H. Zhou, L. Holleis, Y. Saito, L. Cohen, W. Huynh, C. L. Patterson, F. Yang, T. Taniguchi, K. Watanabe, and A. F. Young, Isospin magnetism and spin-polarized superconductivity in Bernal bilayer graphene, *Science* **375**, 774 (2022).
- [15] Y. Zhang, R. Polski, A. Thomson, É. Lantagne-Hurtubise, C. Lewandowski, H. Zhou, K. Watanabe, T. Taniguchi, J. Alicea, and S. Nadj-Perge, Enhanced superconductivity in spin-orbit proximitized bilayer graphene, *Nature (London)* **613**, 268 (2023).
- [16] E. Lake, A. S. Patri, and T. Senthil, Pairing symmetry of twisted bilayer graphene: A phenomenological synthesis, *Phys. Rev. B* **106**, 104506 (2022).
- [17] E. Khalaf, P. Ledwith, and A. Vishwanath, Symmetry constraints on superconductivity in twisted bilayer graphene: Fractional vortices, $4e$ condensates, or nonunitary pairing, *Phys. Rev. B* **105**, 224508 (2022).
- [18] S. Chatterjee, T. Wang, E. Berg, and M. P. Zaletel, Inter-valley coherent order and isospin fluctuation mediated superconductivity in rhombohedral trilayer graphene, *Nat. Commun.* **13**, 6013 (2022).
- [19] A. Ghazaryan, T. Holder, M. Serbyn, and E. Berg, Unconventional Superconductivity in Systems with Annular Fermi Surfaces: Application to Rhombohedral Trilayer Graphene, *Phys. Rev. Lett.* **127**, 247001 (2021).
- [20] M. Oh, K. P. Nuckolls, D. Wong, R. L. Lee, X. Liu, K. Watanabe, T. Taniguchi, and A. Yazdani, Evidence for unconventional superconductivity in twisted bilayer graphene, *Nature (London)* **600**, 240 (2021).
- [21] H. Kim, Y. Choi, C. Lewandowski, A. Thomson, Y. Zhang, R. Polski, K. Watanabe, T. Taniguchi, J. Alicea, and S. Nadj-Perge, Evidence for unconventional superconductivity in twisted trilayer graphene, *Nature (London)* **606**, 494 (2022).
- [22] Y. Cao, D. Rodan-Legrain, J. M. Park, N. F. Yuan, K. Watanabe, T. Taniguchi, R. M. Fernandes, L. Fu, and P. Jarillo-Herrero, Nematicity and competing orders in superconducting magic-angle graphene, *Science* **372**, 264 (2021).
- [23] F. K. de Vries, E. Portolés, G. Zheng, T. Taniguchi, K. Watanabe, T. Ihn, K. Ensslin, and P. Rickhaus, Gate-defined Josephson junctions in magic-angle twisted bilayer graphene, *Nat. Nanotechnol.* **16**, 760 (2021).
- [24] D. Rodan-Legrain, Y. Cao, J. M. Park, S. C. de la Barrera, M. T. Randeria, K. Watanabe, T. Taniguchi, and P. Jarillo-Herrero, Highly tunable junctions and non-local Josephson effect in magic-angle graphene tunnelling devices, *Nat. Nanotechnol.* **16**, 769 (2021).
- [25] E. Portolés, S. Iwakiri, G. Zheng, P. Rickhaus, T. Taniguchi, K. Watanabe, T. Ihn, K. Ensslin, and F. K. de Vries, A tunable monolithic squid in twisted bilayer graphene, *Nat. Nanotechnol.* **17**, 1159 (2022).
- [26] J. Díez-Mérida, A. Díez-Carlón, S. Yang, Y.-M. Xie, X.-J. Gao, J. Senior, K. Watanabe, T. Taniguchi, X. Lu, A. P.

- Higginbotham *et al.*, Symmetry-broken Josephson junctions and superconducting diodes in magic-angle twisted bilayer graphene, *Nat. Commun.* **14**, 2396 (2023).
- [27] H. Sainz-Cruz, P. A. Pantaleón, V. T. Phong, A. Jimeno-Pozo, and F. Guinea, Junctions and Superconducting Symmetry in Twisted Bilayer Graphene, *Phys. Rev. Lett.* **131**, 016003 (2003).
- [28] Y.-M. Xie, D. K. Efetov, and K. T. Law, ϕ_0 -Josephson junction in twisted bilayer graphene induced by a valley-polarized state, *Phys. Rev. Res.* **5**, 023029 (2023).
- [29] M. Alvarado, P. Buset, and A. L. Yeyati, Intrinsic non-magnetic ϕ_0 Josephson junctions in twisted bilayer graphene, *Phys. Rev. Res.* **5**, L032033 (2023).
- [30] A. Bille, R. A. Klemm, and K. Scharnberg, Models of c -axis twist Josephson tunneling, *Phys. Rev. B* **64**, 174507 (2001).
- [31] R. A. Klemm, The phase-sensitive c -axis twist experiments on $\text{Bi}_2\text{Sr}_2\text{CaCu}_2\text{O}_{8+\delta}$ and their implications, *Philos. Mag.* **85**, 801 (2005).
- [32] O. Can, T. Tummuru, R. P. Day, I. Elfimov, A. Damascelli, and M. Franz, High-temperature topological superconductivity in twisted double-layer copper oxides, *Nat. Phys.* **17**, 519 (2021).
- [33] P. A. Volkov, S. Y. F. Zhao, N. Poccia, X. Cui, P. Kim, and J. Pixley, Josephson effects in twisted nodal superconductors, [arXiv:2108.13456](https://arxiv.org/abs/2108.13456).
- [34] T. Tummuru, S. Plugge, and M. Franz, Josephson effects in twisted cuprate bilayers, *Phys. Rev. B* **105**, 064501 (2022).
- [35] T. Tummuru, É. Lantagne-Hurtubise, and M. Franz, Twisted multilayer nodal superconductors, *Phys. Rev. B* **106**, 014520 (2022).
- [36] R. Haenel, T. Tummuru, and M. Franz, Incoherent tunneling and topological superconductivity in twisted cuprate bilayers, *Phys. Rev. B* **106**, 104505 (2022).
- [37] X.-Y. Song, Y.-H. Zhang, and A. Vishwanath, Doping a moiré Mott insulator: A $t - j$ model study of twisted cuprates, *Phys. Rev. B* **105**, L201102 (2022).
- [38] Q. Li, Y. N. Tsay, M. Suenaga, R. A. Klemm, G. D. Gu, and N. Koshizuka, $\text{Bi}_2\text{Sr}_2\text{CaCu}_2\text{O}_{8+\delta}$ Bicrystal c -axis Twist Josephson Junctions: A New Phase-Sensitive Test of Order Parameter Symmetry, *Phys. Rev. Lett.* **83**, 4160 (1999).
- [39] S. Y. F. Zhao, N. Poccia, X. Cui, P. A. Volkov, H. Yoo, R. Engelke, Y. Ronen, R. Zhong, G. Gu, S. Plugge, T. Tummuru, M. Franz, J. H. Pixley, and P. Kim, Emergent interfacial superconductivity between twisted cuprate superconductors, [arXiv:2108.13455](https://arxiv.org/abs/2108.13455).
- [40] Y. Zhu, H. Wang, Z. Wang, S. Hu, G. Gu, J. Zhu, D. Zhang, and Q.-K. Xue, Persistent Josephson tunneling between $\text{Bi}_2\text{Sr}_2\text{CaCu}_2\text{O}_{8+x}$ flakes twisted by 45° across the superconducting dome, [arXiv:2301.03838](https://arxiv.org/abs/2301.03838).
- [41] M. Martini, Y. Lee, T. Confalone, S. Shokri, C. N. Saggau, D. Wolf, G. Gu, K. Watanabe, T. Taniguchi, D. Montemurro *et al.*, Twisted cuprate van der Waals heterostructures with controlled Josephson coupling, *Mater. Today* **67**, 106 (2023).
- [42] L. Britnell, R. Gorbachev, A. Geim, L. Ponomarenko, A. Mishchenko, M. Greenaway, T. Fromhold, K. Novoselov, and L. Eaves, Resonant tunnelling and negative differential conductance in graphene transistors, *Nat. Commun.* **4**, 1794 (2013).
- [43] A. Mishchenko, J. Tu, Y. Cao, R. V. Gorbachev, J. Wallbank, M. Greenaway, V. Morozov, S. Morozov, M. Zhu, S. Wong *et al.*, Twist-controlled resonant tunnelling in graphene/boron nitride/graphene heterostructures, *Nat. Nanotechnol.* **9**, 808 (2014).
- [44] A. Inbar, J. Birkbeck, J. Xiao, T. Taniguchi, K. Watanabe, B. Yan, Y. Oreg, A. Stern, E. Berg, and S. Ilani, The quantum twisting microscope, *Nature (London)* **614**, 682 (2023).
- [45] R. Bistritzer and A. H. MacDonald, Moiré bands in twisted double-layer graphene, *Proc. Natl. Acad. Sci. USA* **108**, 12233 (2011).
- [46] V. Ambegaokar and A. Baratoff, Tunneling Between Superconductors, *Phys. Rev. Lett.* **10**, 486 (1963).
- [47] K. Jiang and J. Hu, Superconducting diode effects, *Nat. Phys.* **18**, 1145 (2022).
- [48] G.-B. Liu, W.-Y. Shan, Y. Yao, W. Yao, and D. Xiao, Three-band tight-binding model for monolayers of group-VIB transition metal dichalcogenides, *Phys. Rev. B* **88**, 085433 (2013).
- [49] P. A. Volkov, É. Lantagne-Hurtubise, T. Tummuru, J. H. Pixley, S. Plugge, and M. Franz, Josephson diode effects in twisted nodal superconductors, [arXiv:2307.01261](https://arxiv.org/abs/2307.01261).
- [50] H. S. Arora, R. Polski, Y. Zhang, A. Thomson, Y. Choi, H. Kim, Z. Lin, I. Z. Wilson, X. Xu, J.-H. Chu *et al.*, Superconductivity in metallic twisted bilayer graphene stabilized by WSe_2 , *Nature (London)* **583**, 379 (2020).
- [51] G. Kresse and J. Furthmüller, Efficiency of ab-initio total energy calculations for metals and semiconductors using a plane-wave basis set, *Comput. Mater. Sci.* **6**, 15 (1996).
- [52] G. Kresse and J. Furthmüller, Efficient iterative schemes for *ab initio* total-energy calculations using a plane-wave basis set, *Phys. Rev. B* **54**, 11169 (1996).
- [53] J. P. Perdew, K. Burke, and M. Ernzerhof, Generalized Gradient Approximation made Simple, *Phys. Rev. Lett.* **77**, 3865 (1996).
- [54] A. Barone and G. Paterno, *Physics and Applications of the Josephson Effect* (Wiley Online Library, 1982), Vol. 1.